Supplementary Information

Article title

Non-destructive degradation pattern decoupling for early battery trajectory prediction via physics-informed learning

Author information

Shengyu Tao[1, 6, #], Mengtian Zhang[1, #], Zixi Zhao[1, #], Haoyang Li[2], Ruifei Ma[1], Yunhong Che[3], Xin Sun[4], Lin Su[1], Chongbo Sun[1], Xiangyu Chen[1], Heng Chang[1], Shiji Zhou[1], Zepeng Li[1], Hanyang Lin[1], Yaojun Liu[5], Wenjun Yu[5], Zhongling Xu[5], Han Hao[2], Scott Moura[6], Xuan Zhang[1, *], Yang Li[1, *], Xiaosong Hu[7, *], Guangmin Zhou[1,*]

1. Tsinghua-Berkeley Shenzhen Institute & Tsinghua Shenzhen International Graduate School, Tsinghua University, Shenzhen, China
2. State Key Laboratory of Intelligent Green Vehicle and Mobility, Tsinghua University, Beijing, China
3. Department of Energy, Aalborg University, Aalborg, Denmark
4. Integrated Research on Energy, Environment and Society (IREES), Energy and Sustainability Research Institute Groningen (ESRIG), University of Groningen, Groningen, the Netherlands
5. Sunwoda Mobility Energy Technology Co., Ltd., Shenzhen, China
6. Energy, Controls and Applications Lab (eCAL), Department of Civil and Environmental Engineering, University of California, Berkeley, California, USA
7. College of Mechanical and Vehicle Engineering, Chongqing University, Chongqing, China

#These authors were of equal contributions.
*Correspondence to whom should be addressed.

This supplementary information file contains:
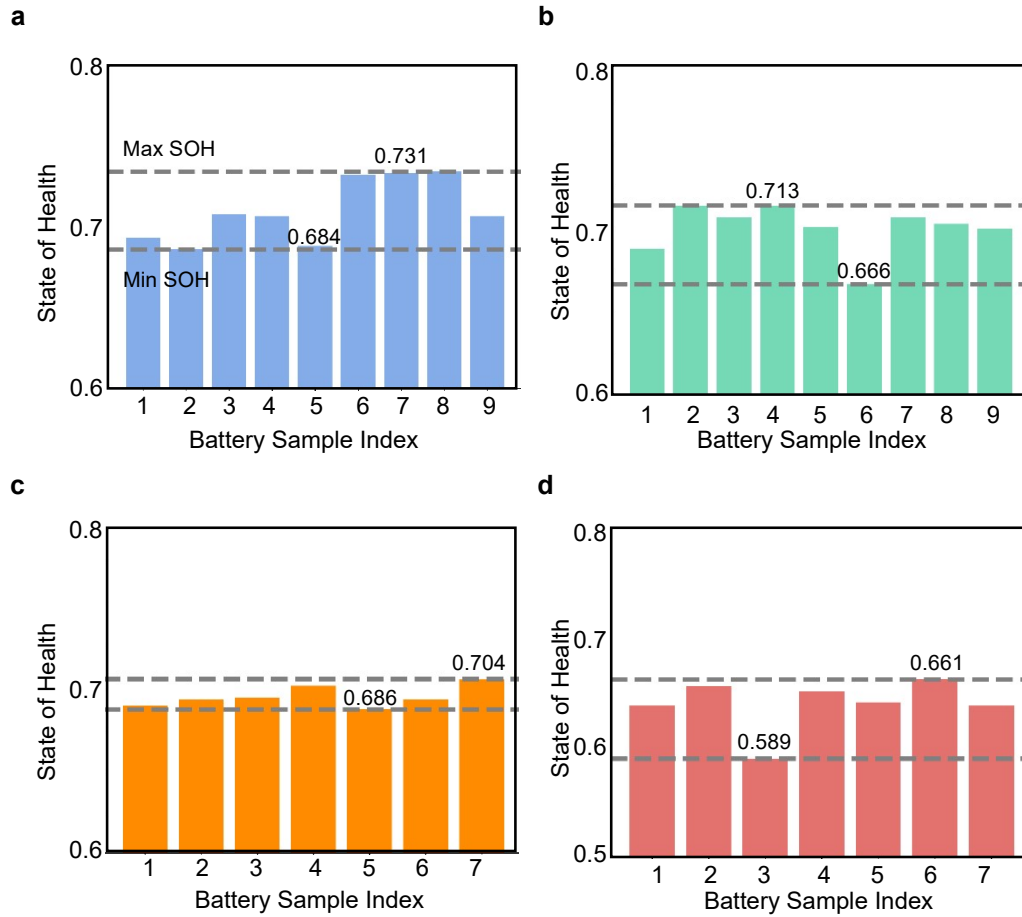
Supplementary Figures 1 to 40

Supplementary Tables 1 to 6

Supplementary Notes 1 to 10

Supplementary Discussion 1

Supplementary Figure 1

Battery state of health (SOH) distribution under (a) 25, (b) 35, (c) 45, and (d) 55 $^\circ$C when the cycling tests end, with the maximum and minimum SOH lines indicated for each temperature. There are 9, 9, 7, and 7 battery samples under test for 25, 35, 45, and 55 $^\circ$C, respectively.
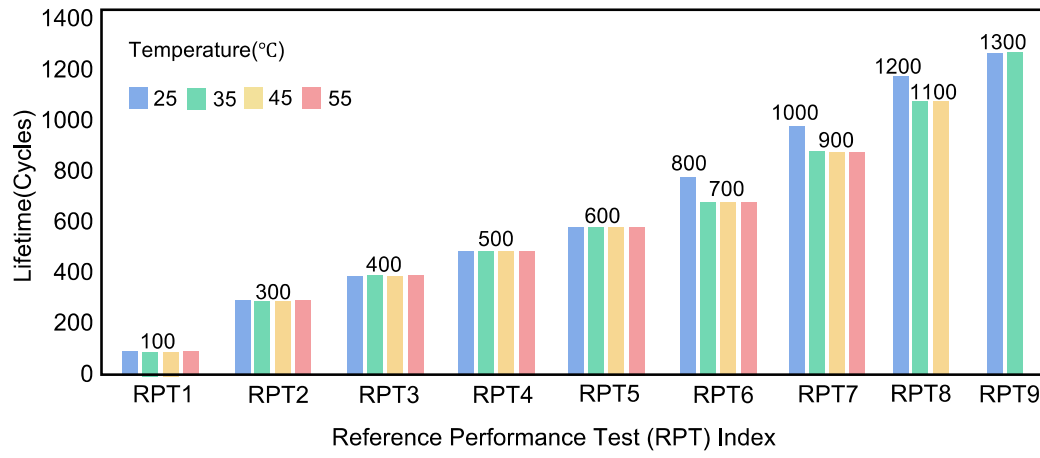
Supplementary Figure 2

Battery lifetime distribution at 80% of the nominal capacity (1.1Ah), i.e., EOL80 definition. Lifetime distribution under (a) 25, (b) 35, (c) 45, (d) 55 °C, and (e) all temperatures, with mean lifetime (Mean value) and lifetime standard deviation (Std value) indicated. There are 9, 9, 7, and 7 battery samples under test for 25, 35, 45, and 55 °C, respectively.
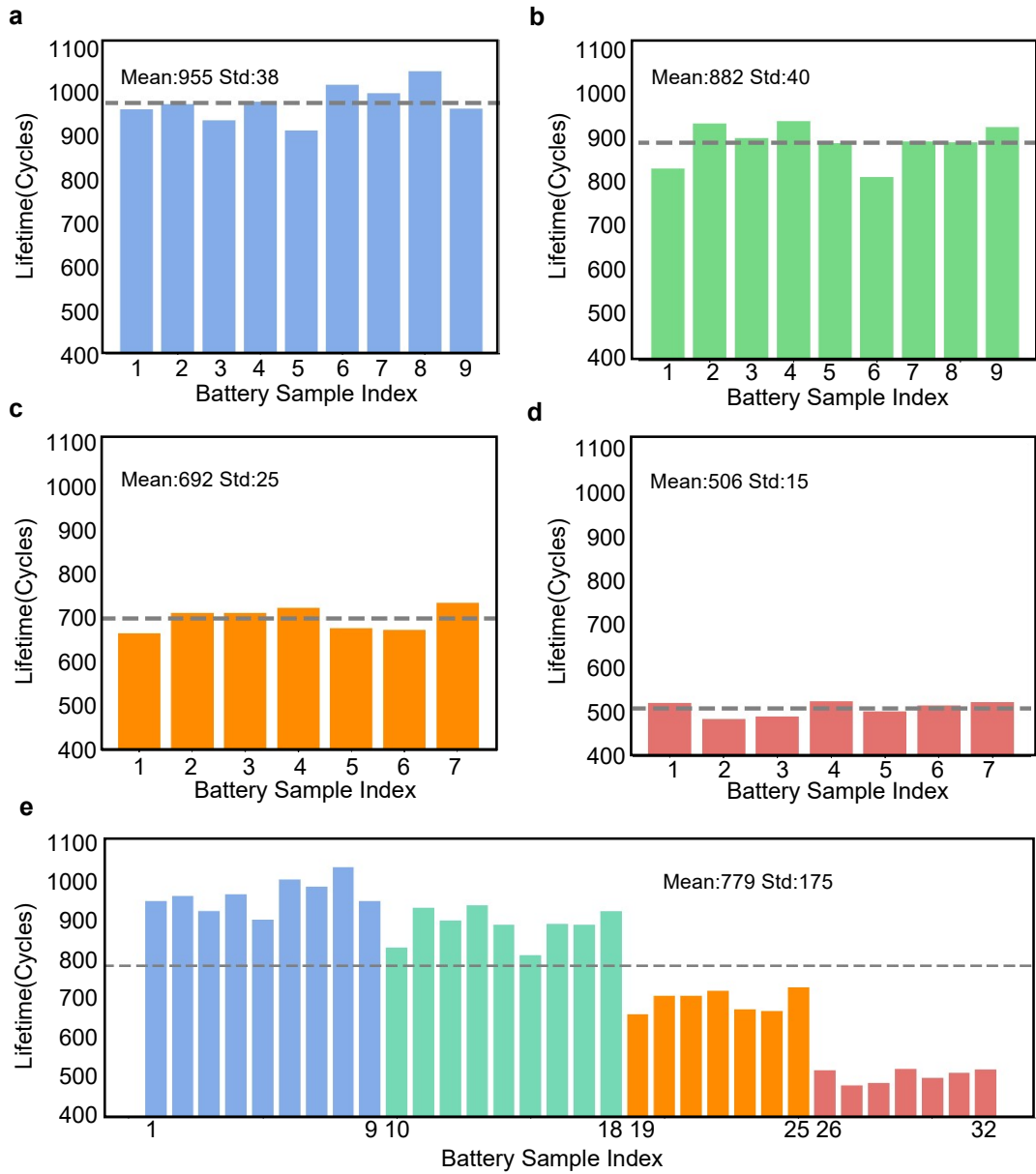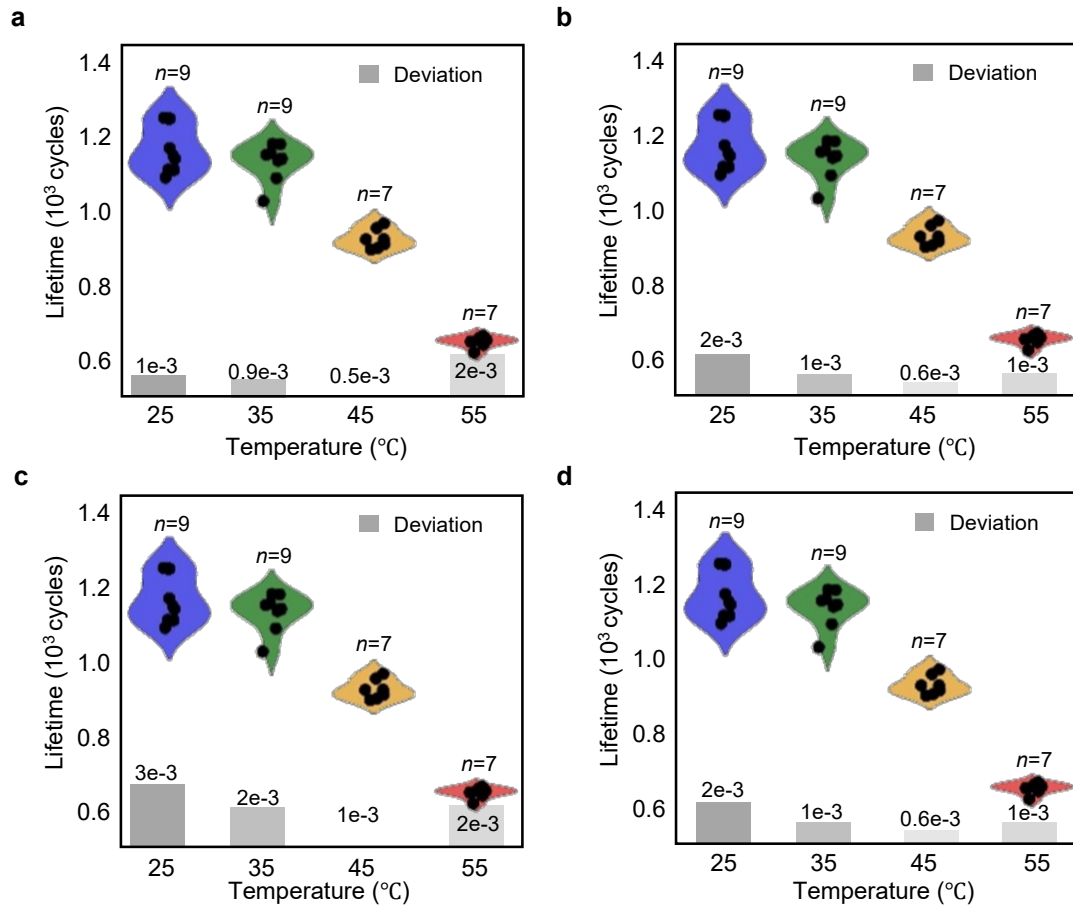
Supplementary Figure 3

Illustration of the time for reference performance test (RPT) for batteries. Batteries under high temperatures are of fewer RPTs due to a shortened lifetime.

Supplementary Figure 4

Macro lifetime deviations at the (a) 25th cycle, (b) 50th cycle, (c) 75th cycle, and (d) 100th cycle for all batteries, indicated by the bar plots. The lifetime distributions at 0.8Ah, i.e., 73% of the nominal capacity are illustrated by violin plots to demonstrate deviations are being amplified during cycling, even though the temperature condition and cycling schemes are identical.

Supplementary Figure 5

Correlation between stepwise IMVs and battery capacity deviation at the (a) 25th and (b) 50th (c) 100th cycle for all batteries. (d) Correlation evolution in lifetime direction with a resolution of 5 cycles. IMV values are averaged over batteries at each temperature, respectively. The least square regression is performed to determine the correlation between capacity deviation and IMVs at all temperatures.
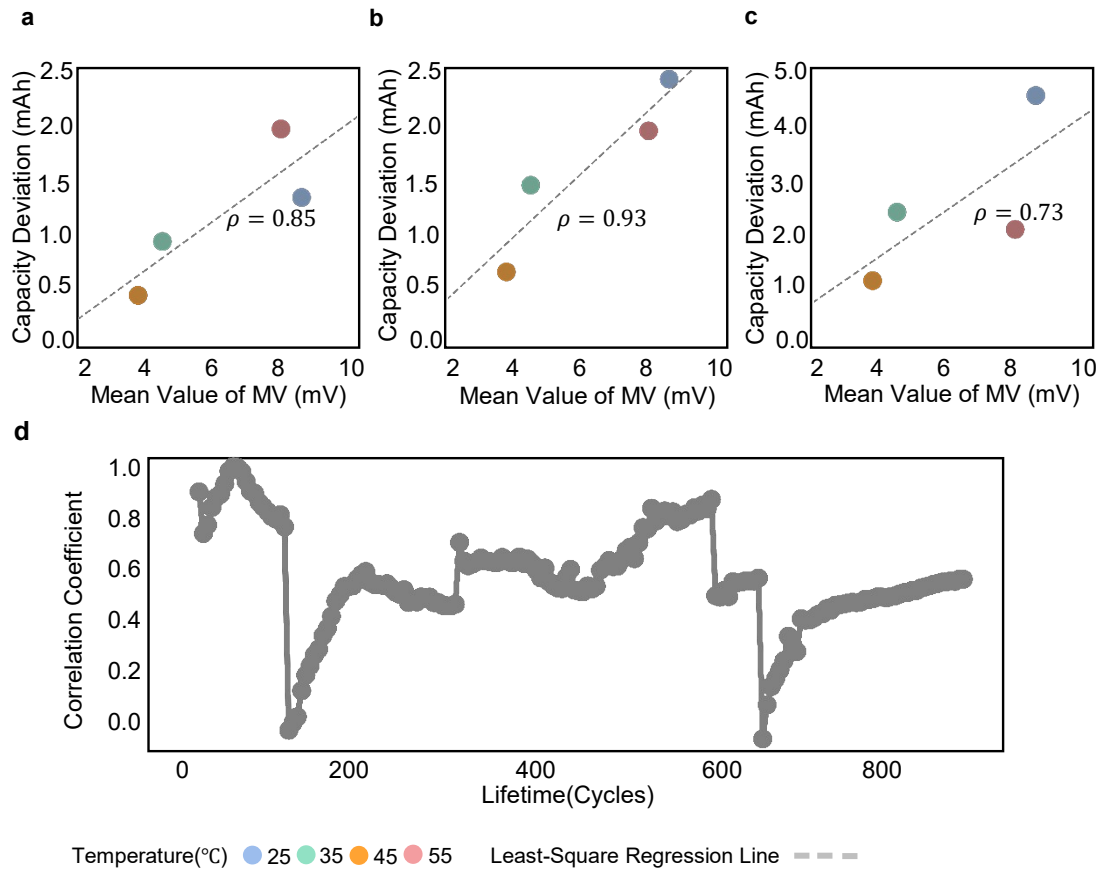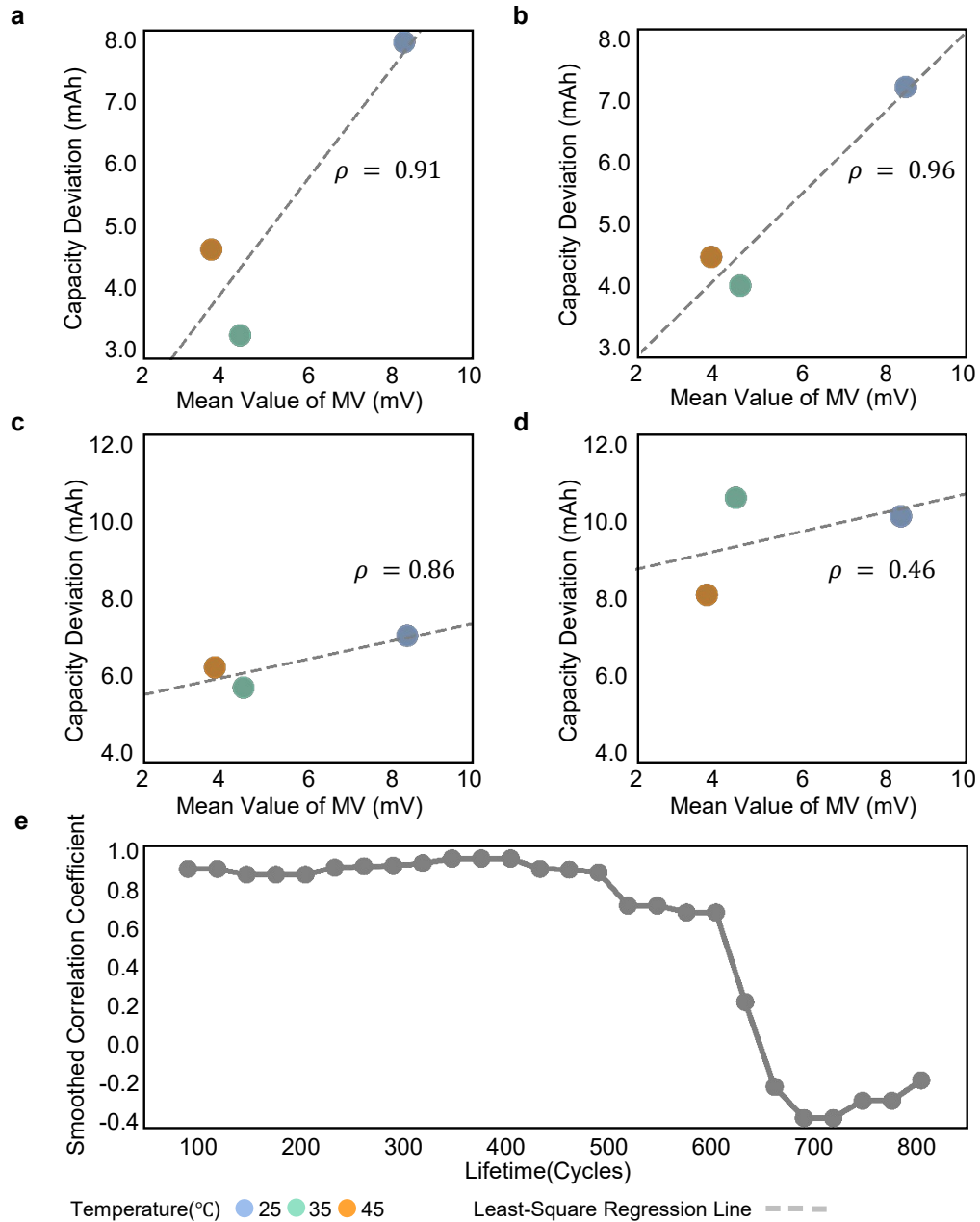
Supplementary Figure 6

Correlation between stepwise IMVs and battery capacity deviation at the (a) 200th and (b) 400th (c) 600th and (d) 900th cycle. (e) Correlation evolution in lifetime direction with a resolution of 30 cycles, which is further smoothed with a window of 5 to reduce the influence of outliers. IMV values are averaged over batteries at each temperature, excluding IMVs at 55°C., respectively. The least square regression is performed to determine the correlation between capacity deviation and IMVs at 25, 35, and 45°C.

Supplementary Figure 7

Charging dynamics, i.e., voltage response curve against the state of charge (SOC), in each charging step, from (a) to (i) at 25°C. The lifetime variation of the charging dynamics is mapped by colors for the visibility of its trend in the lifetime direction.
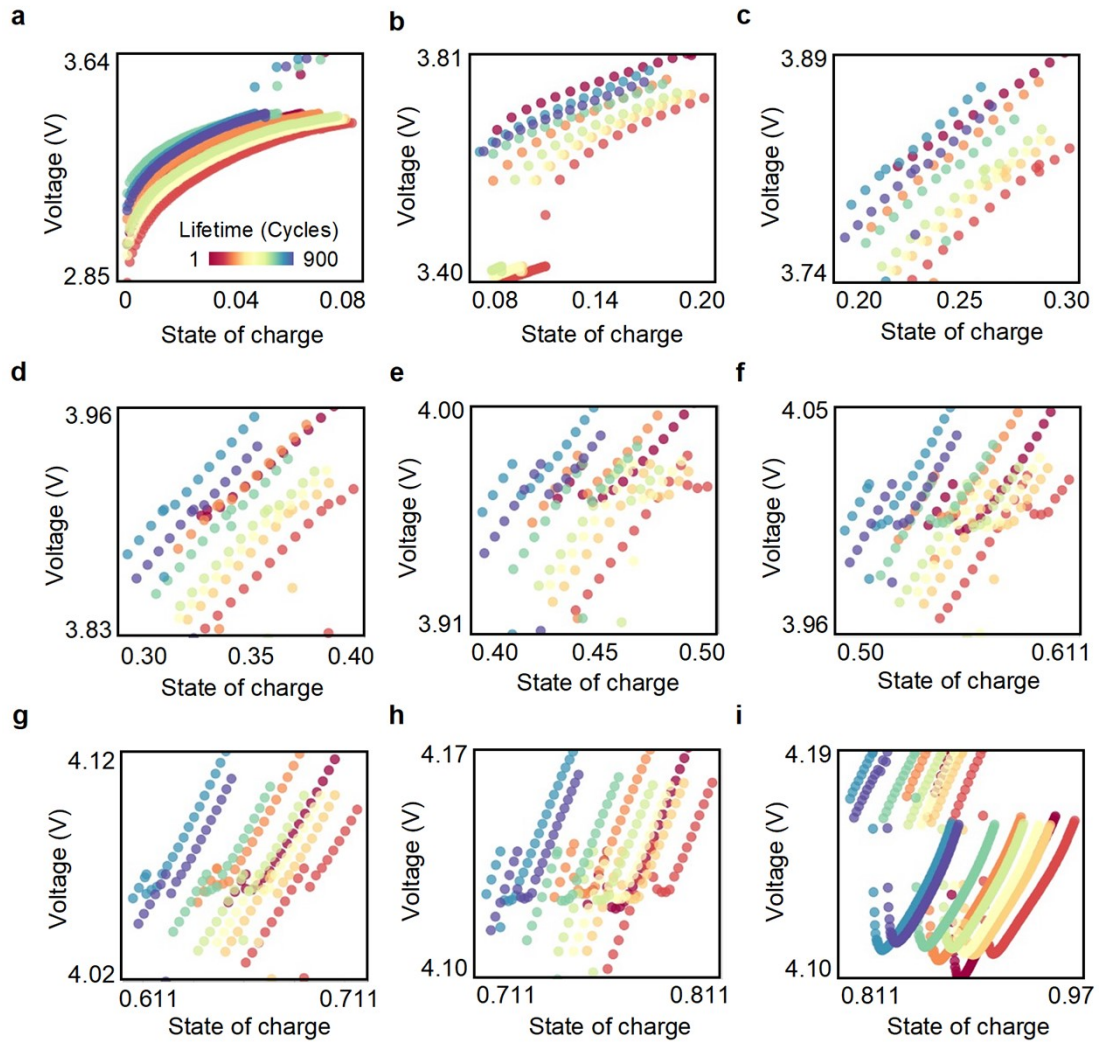
Supplementary Figure 8

Charging dynamics, i.e., voltage response curve against the state of charge (SOC), in each charging step, from (a) to (i) at 35°C. The lifetime variation of the charging dynamics is mapped by colors for the visibility of its trend in the lifetime direction.

Supplementary Figure 9

Charging dynamics, i.e., voltage response curve against the state of charge (SOC), in each charging step, from (a) to (i) at $45^{\circ}C$. The lifetime variation of the charging dynamics is mapped by colors for the visibility of its trend in the lifetime direction.
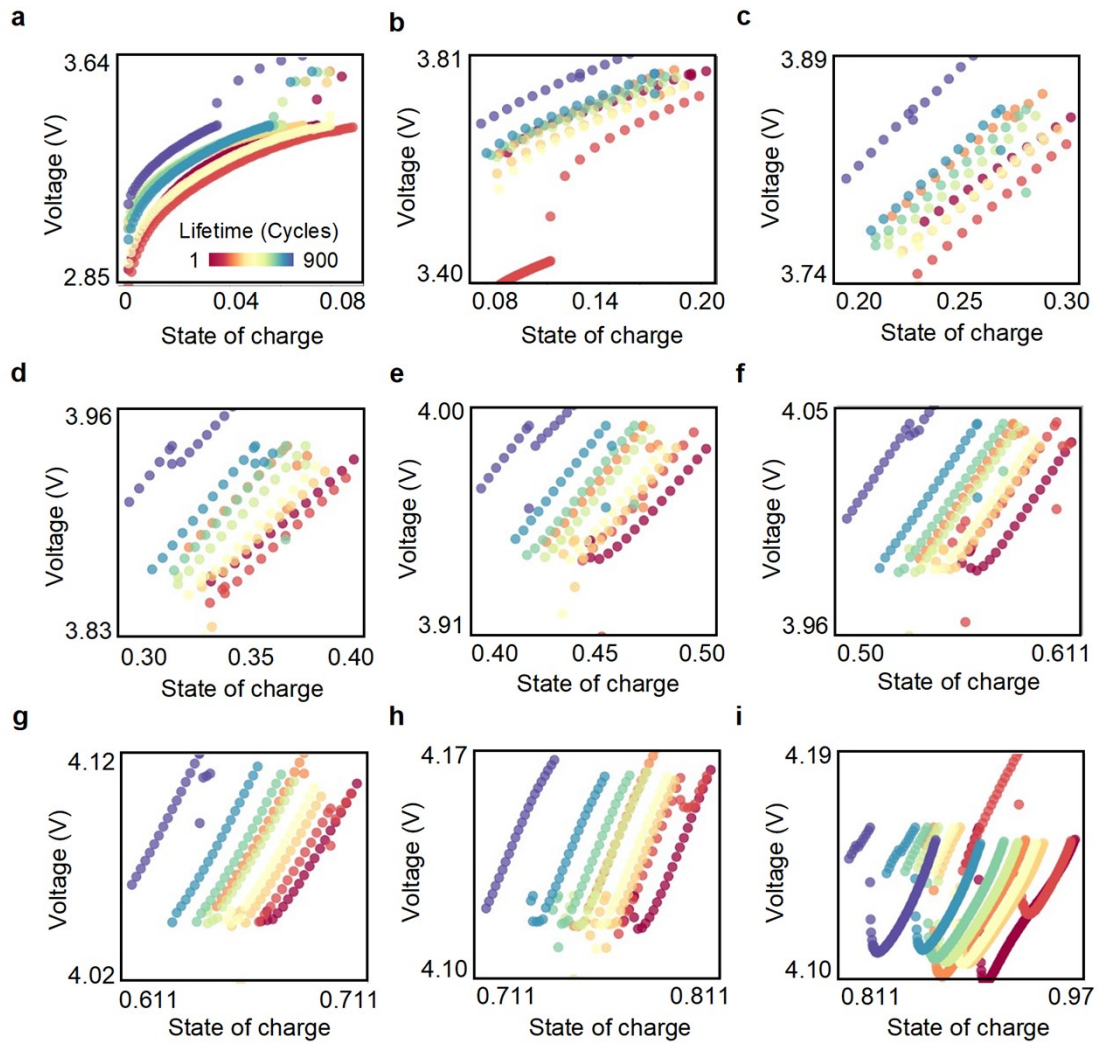
Supplementary Figure 10

Charging dynamics, i.e., voltage response curve against the state of charge (SOC), in each charging step, from (a) to (i) at 55°C. The lifetime variation of the charging dynamics is mapped by colors for the visibility of its trend in the lifetime direction.
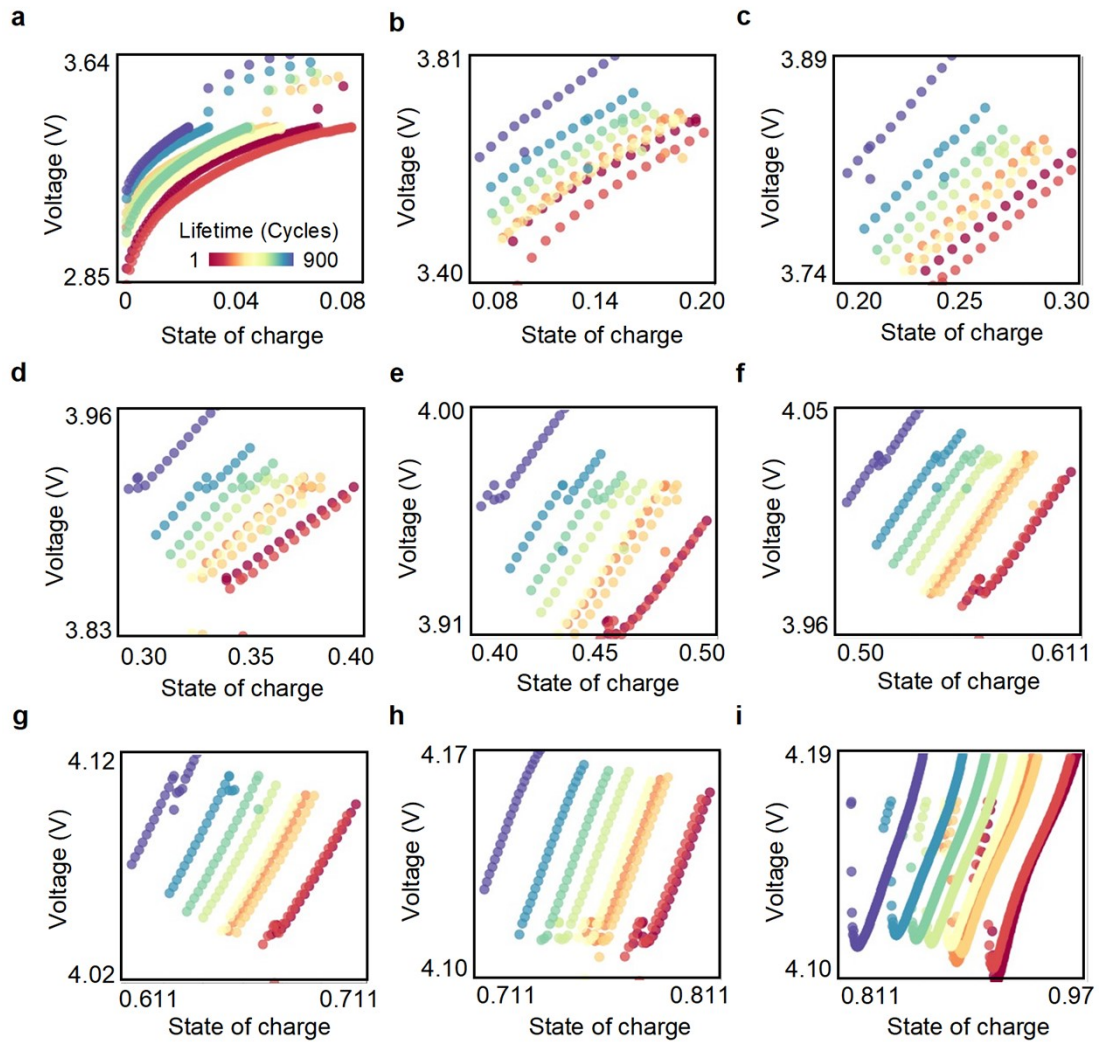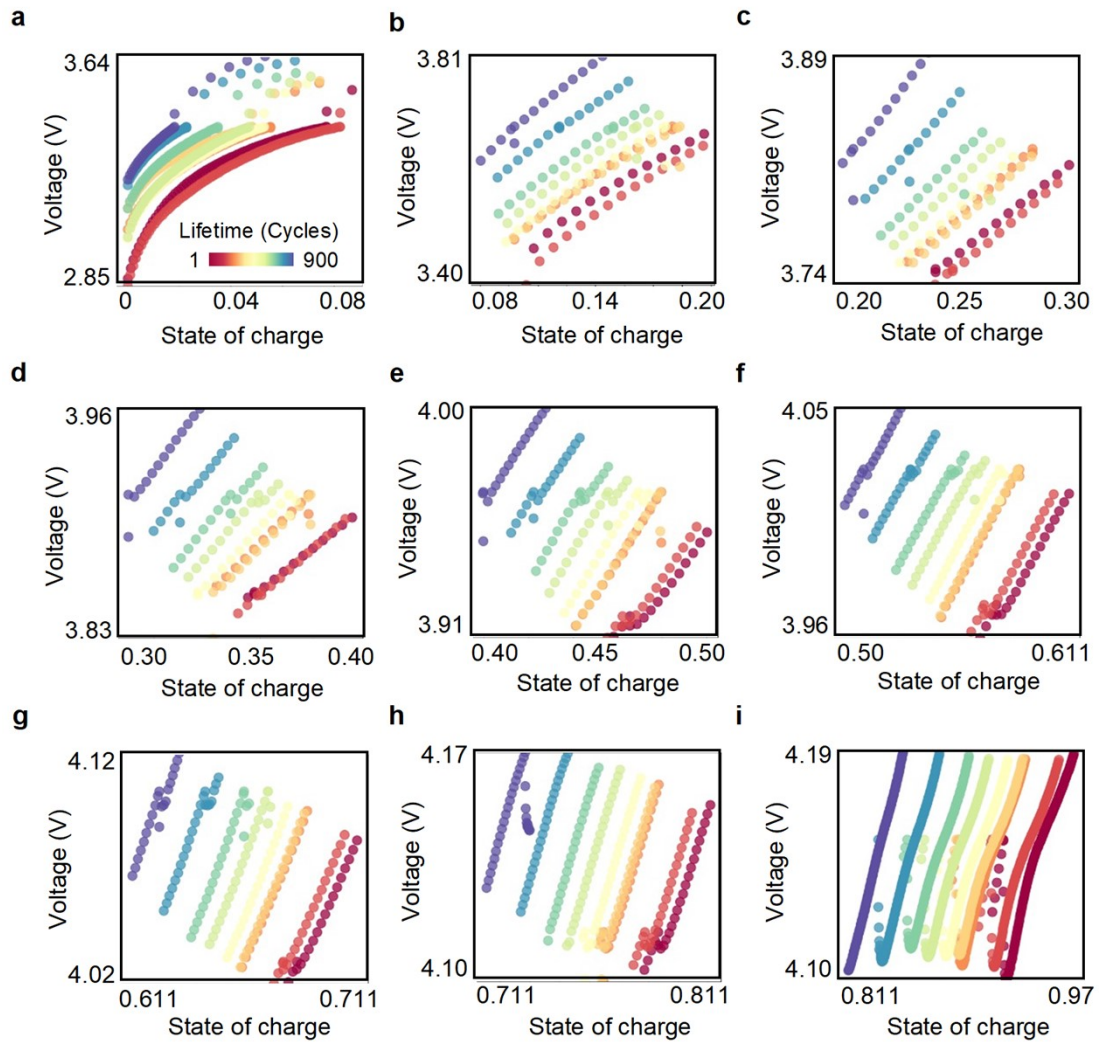
Supplementary Figure 11

The ohmic resistance (RO) and stability (battery-wise standard deviation) evolution in lifetime direction for each charging stage at 25°C. (a-h) are for RO in each charging switching point.
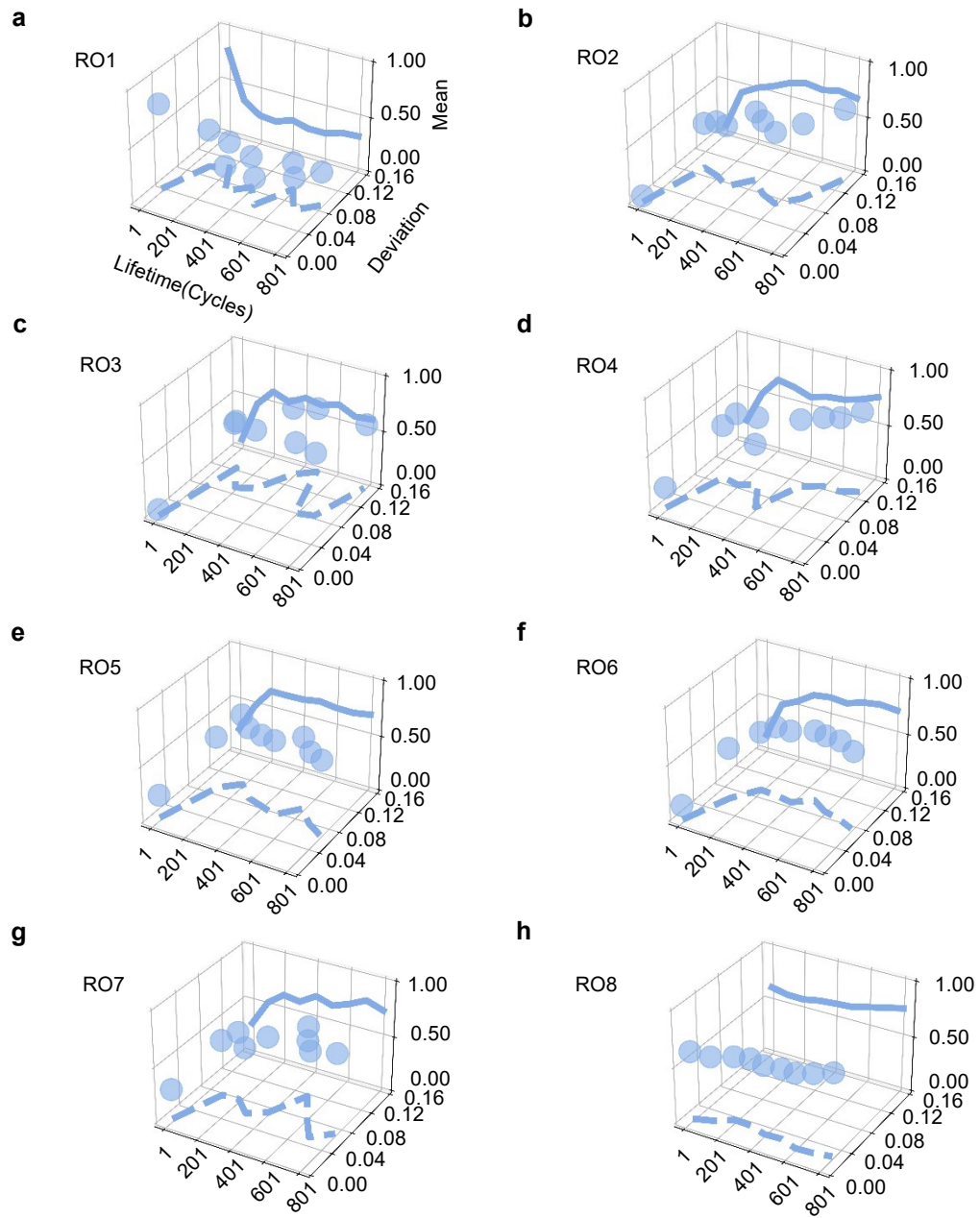
Supplementary Figure 12

The ohmic resistance (RO) and stability (battery-wise standard deviation) evolution in lifetime direction for each charging stage at 35°C. (a-h) are for RO in each charging switching point.

Supplementary Figure 13

The ohmic resistance (RO) and stability (battery-wise standard deviation) evolution in lifetime direction for each charging stage at 45°C. (a-h) are for RO in each charging switching point.

Supplementary Figure 14

The ohmic resistance (RO) and stability (battery-wise standard deviation) evolution in lifetime direction for each charging stage at $55^\circ C$. (a-h) are for RO in each charging switching point.
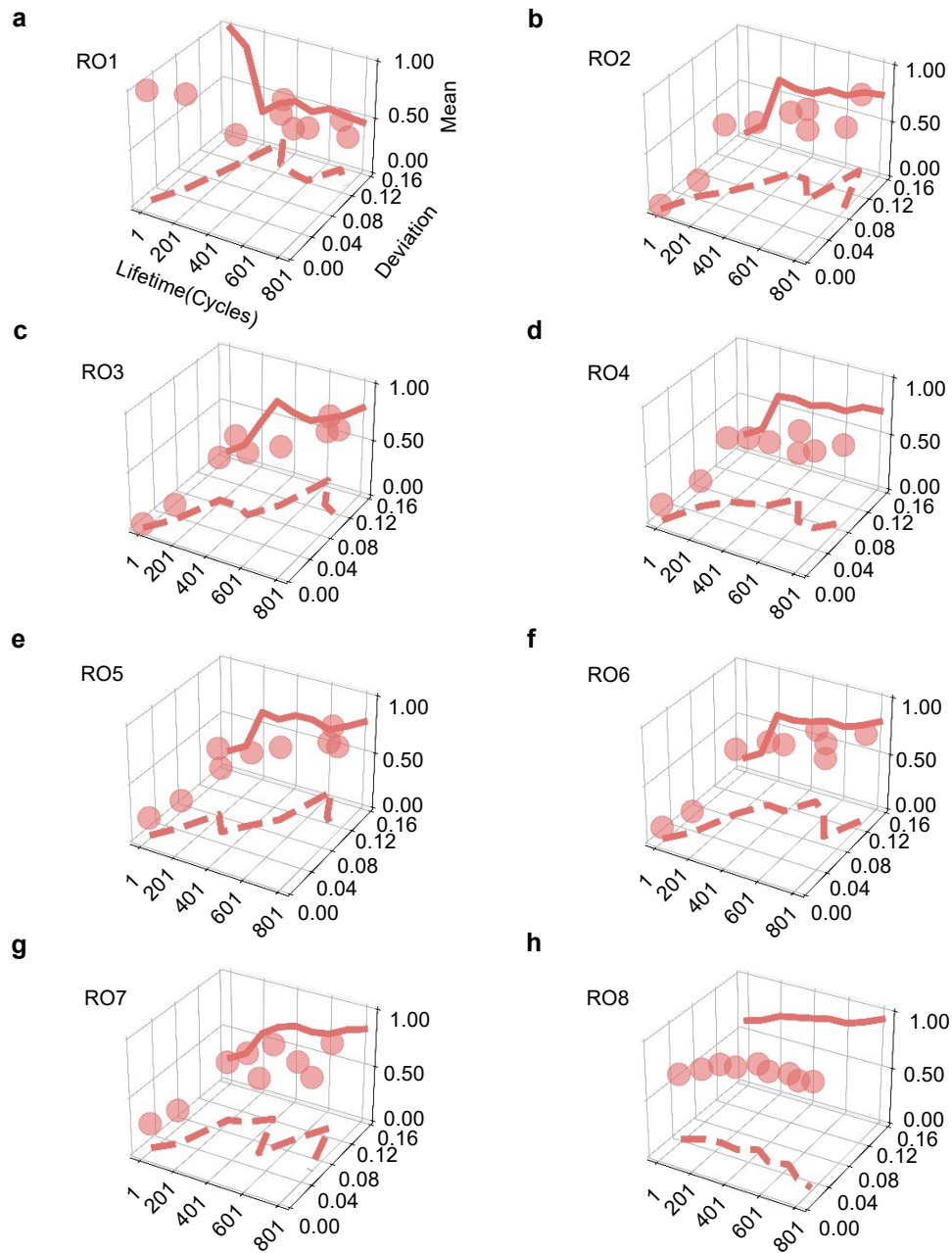
Supplementary Figure 15

The lumped resistance (RL) and stability (battery-wise standard deviation) evolution in lifetime direction for each charging stage at 25°C. (a-i) are for RL in each charging step.
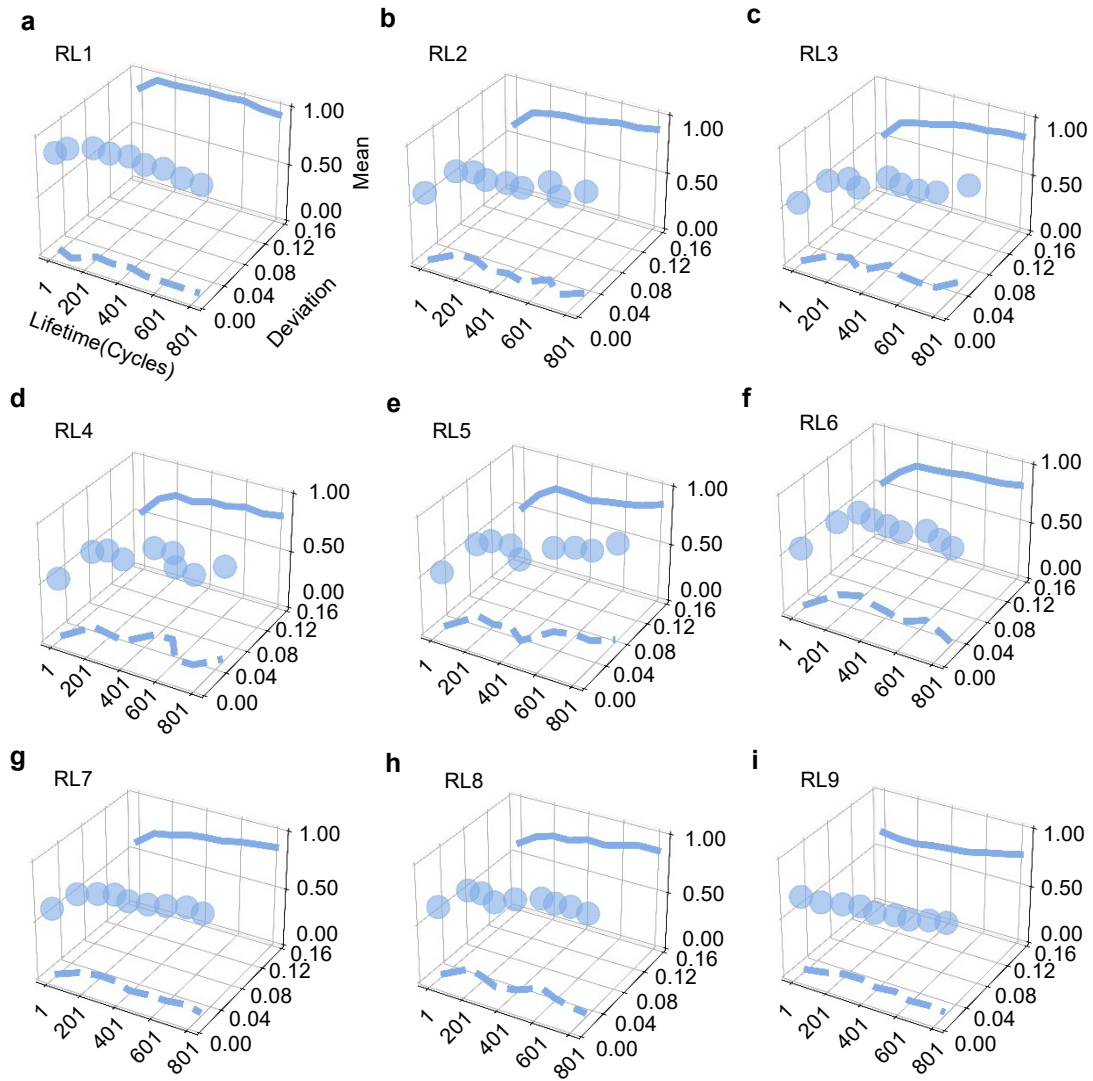
Supplementary Figure 16

The lumped resistance (RL) and stability (battery-wise standard deviation) evolution in lifetime direction for each charging stage at 35°C. (a-i) are for RL in each charging step.
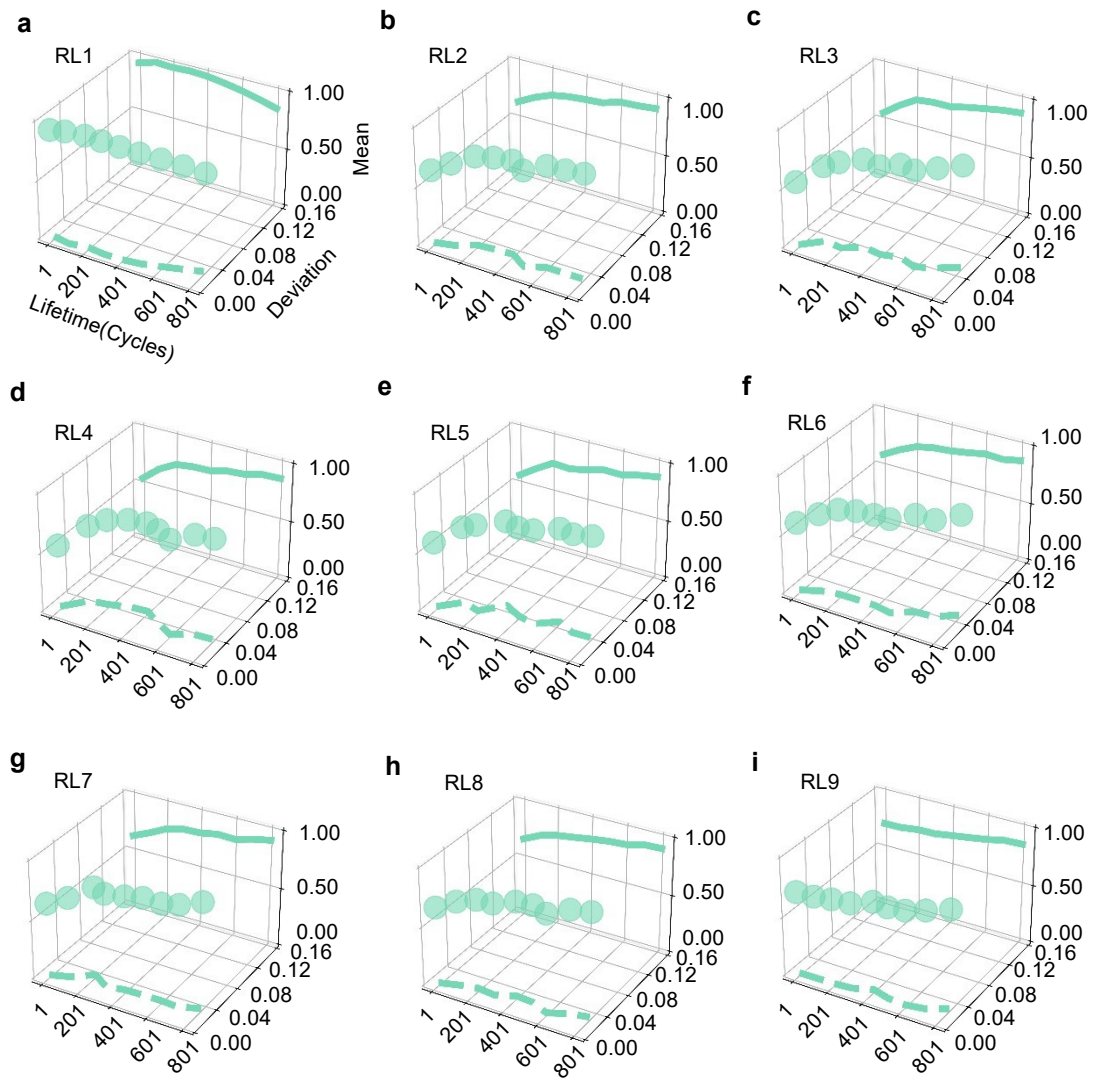
Supplementary Figure 17

The lumped resistance (RL) and stability (battery-wise standard deviation) evolution in lifetime direction for each charging stage at 45°C. (a-i) are for RL in each charging step.
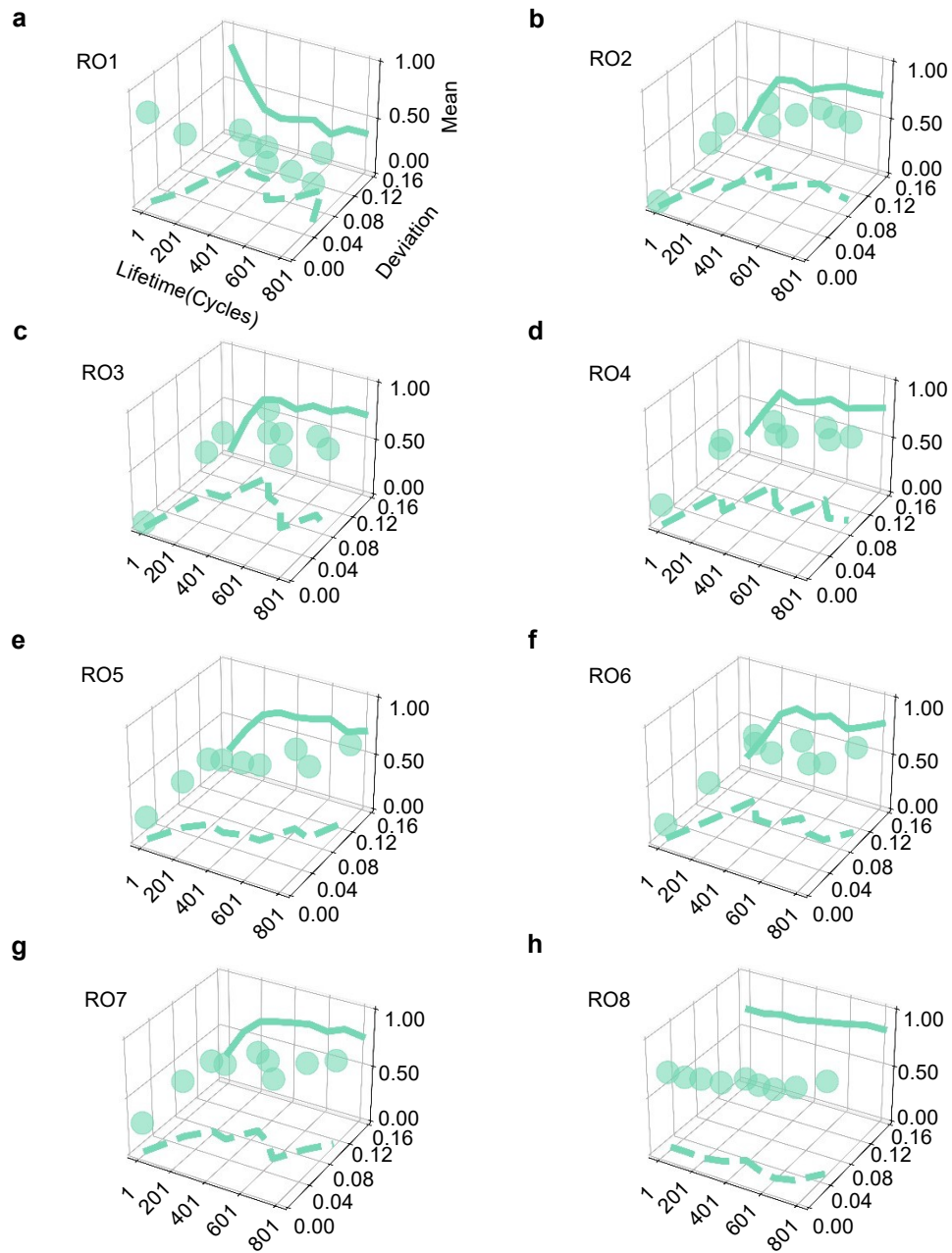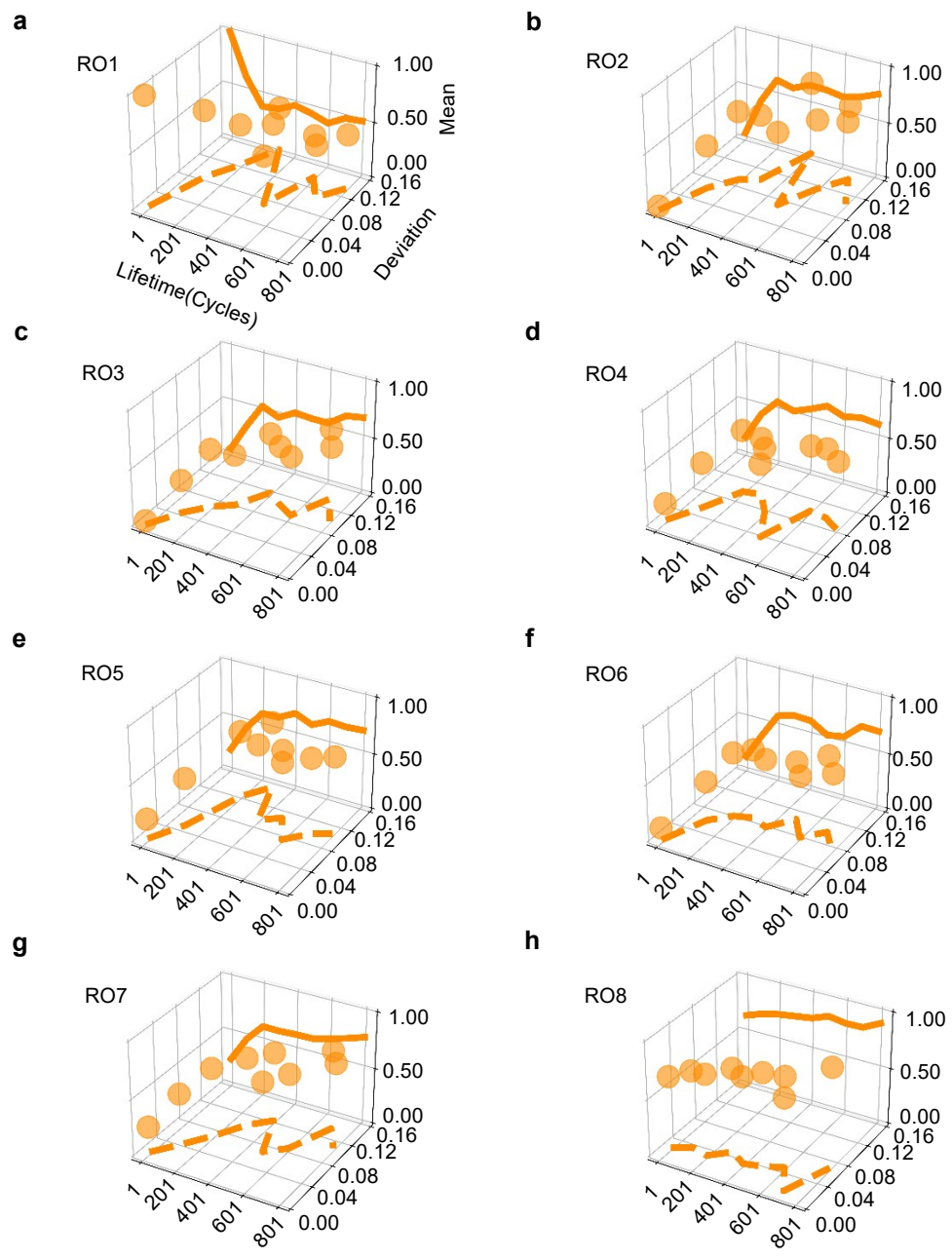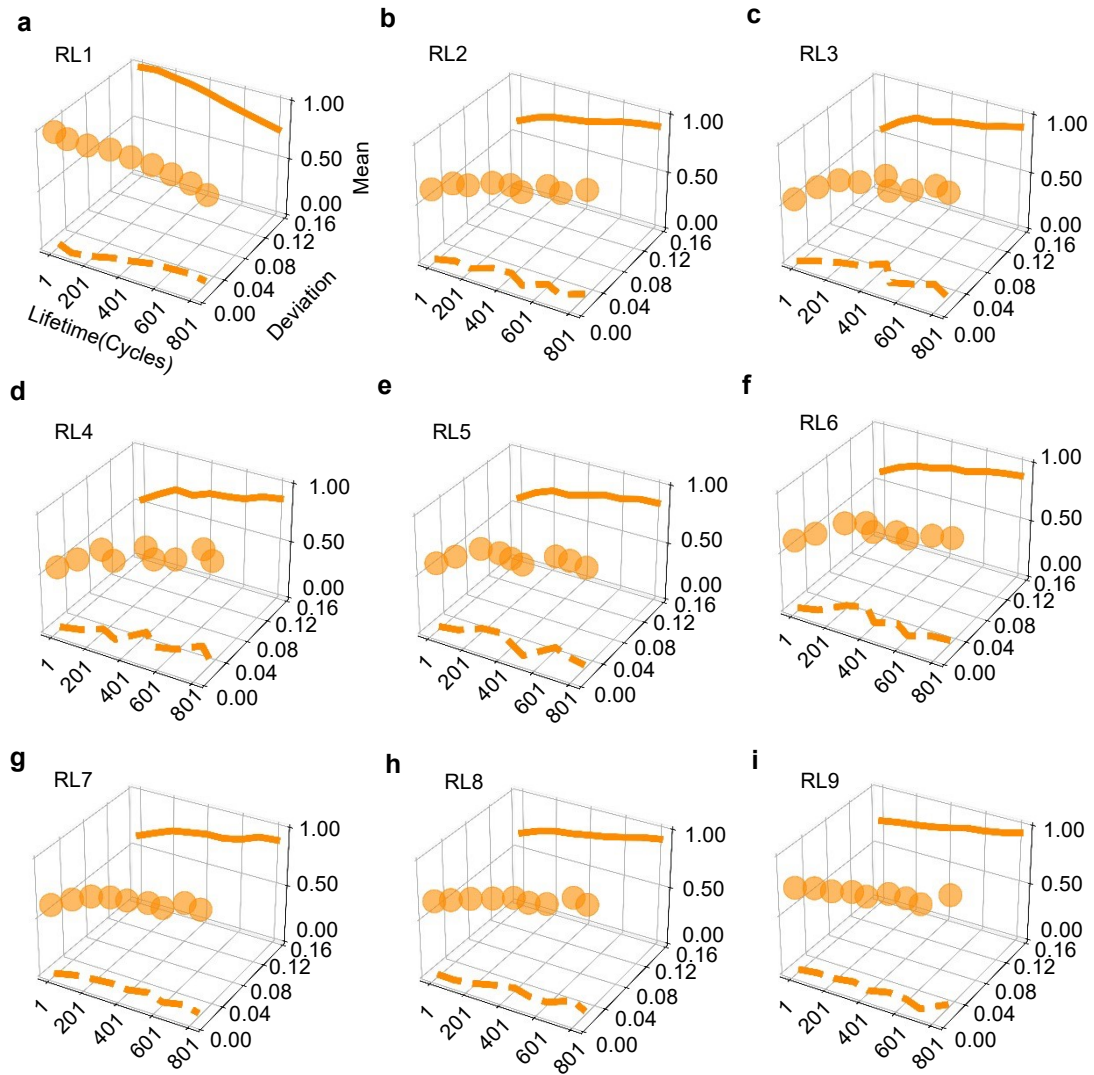
Supplementary Figure 18

The lumped resistance (RL) and stability (battery-wise standard deviation) evolution in lifetime direction for each charging stage at 55°C. (a-i) are for RL in each charging step.
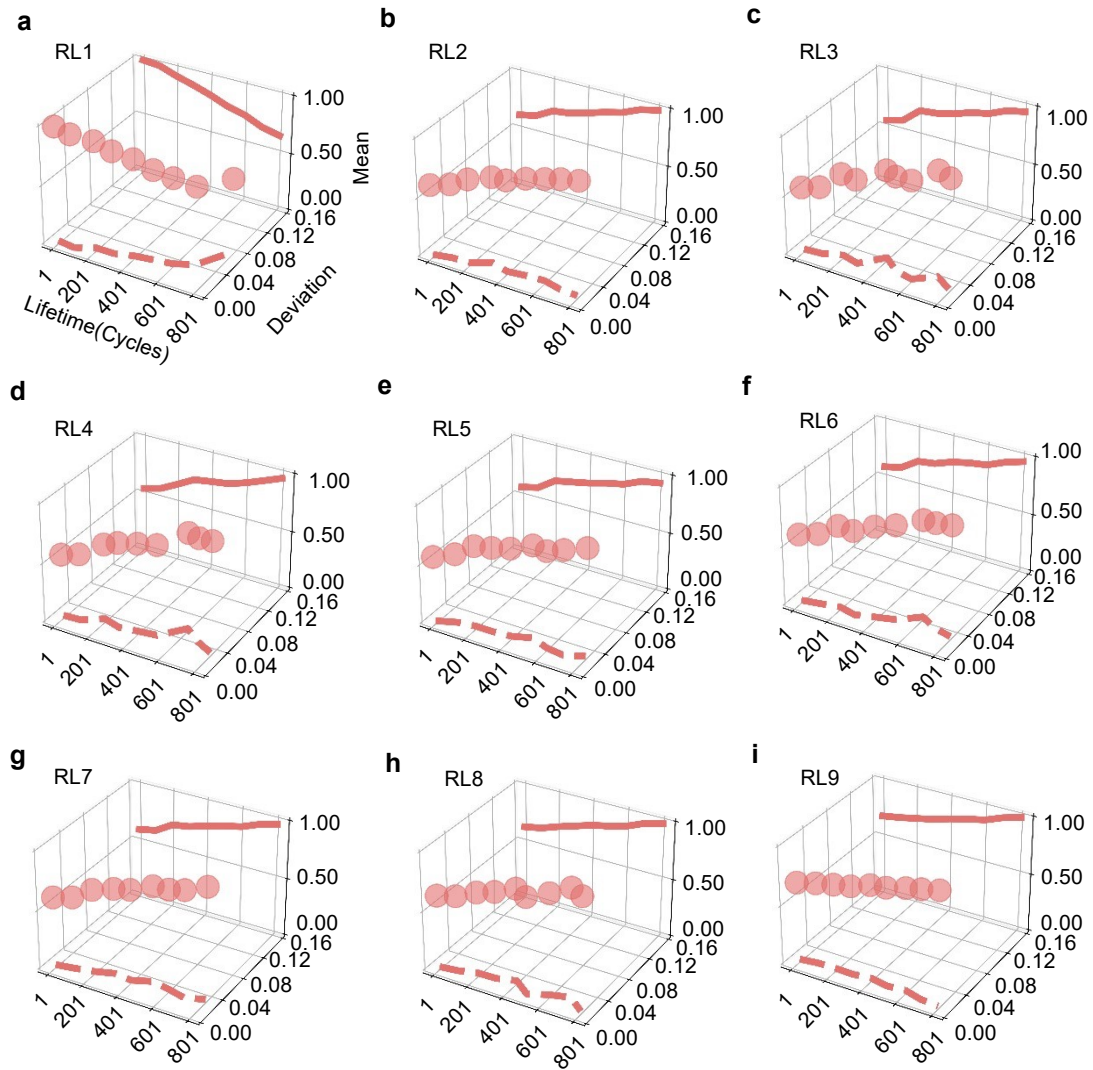
Supplementary Figure 19

The charging capacity (Q), polarization speed (Vg), and their stabilities (battery-wise standard deviation) evolution in lifetime direction for each charging stage at 25°C, respectively. (a-i) are for Q and Vg in each charging step, respectively.
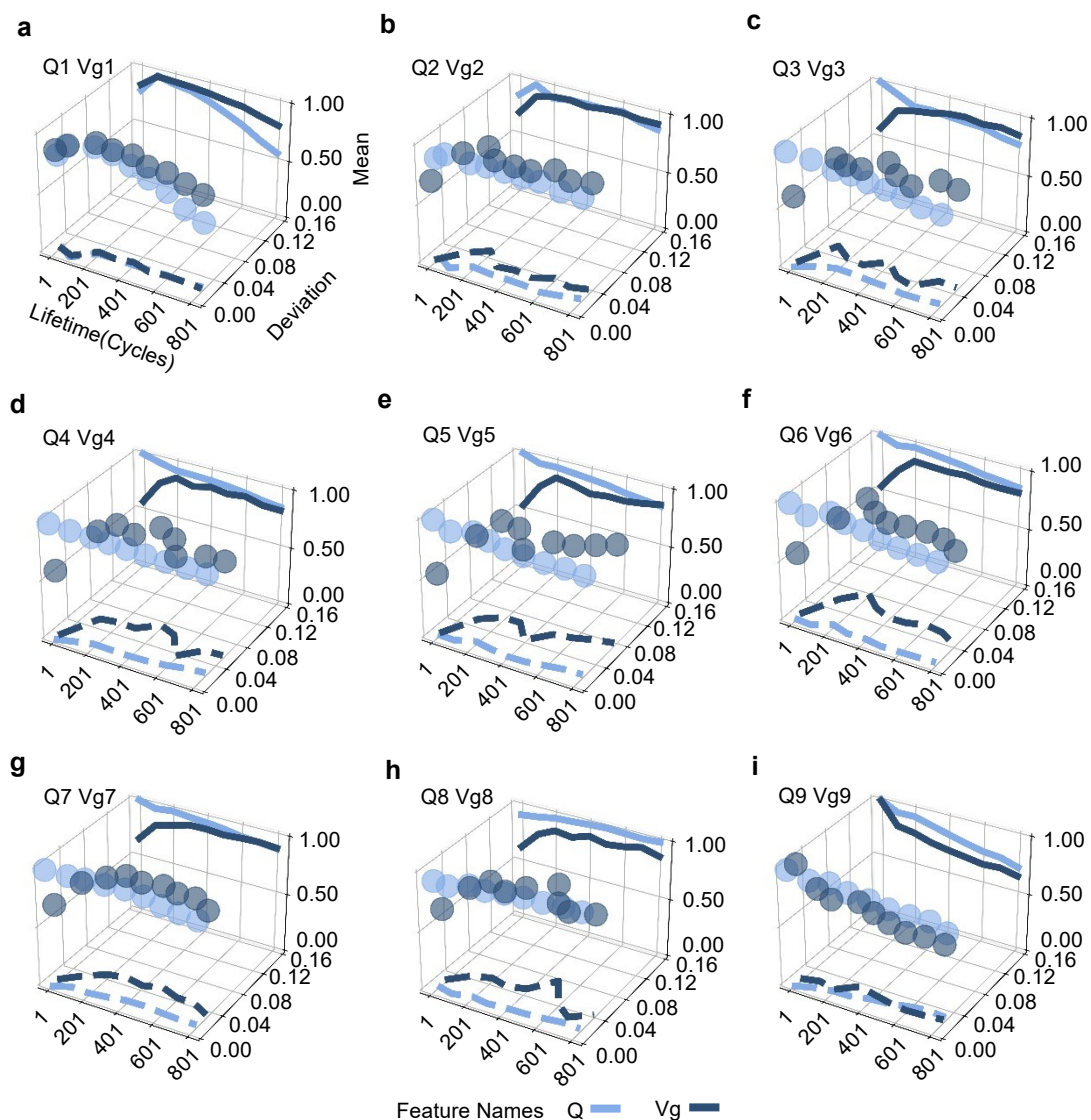
Supplementary Figure 20

The charging capacity (Q), polarization speed (Vg), and their stabilities (battery-wise standard deviation) evolution in lifetime direction for each charging stage at 35℃, respectively. (a-i) are for Q and Vg in each charging step, respectively.
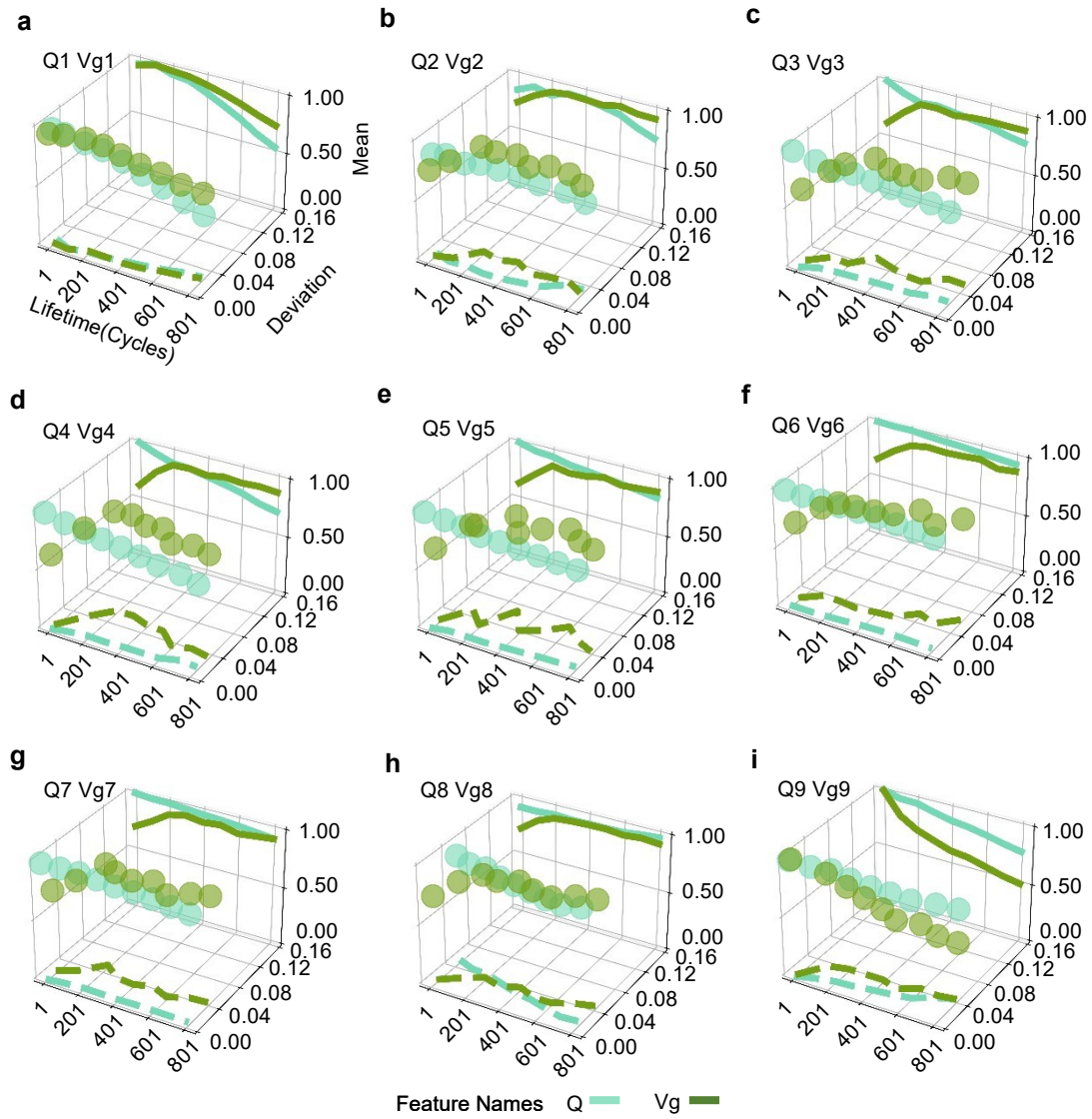
Supplementary Figure 21

The charging capacity (Q), polarization speed (Vg), and their stabilities (battery-wise standard deviation) evolution in lifetime direction for each charging stage at 45℃, respectively. (a-i) are for Q and Vg in each charging step, respectively.
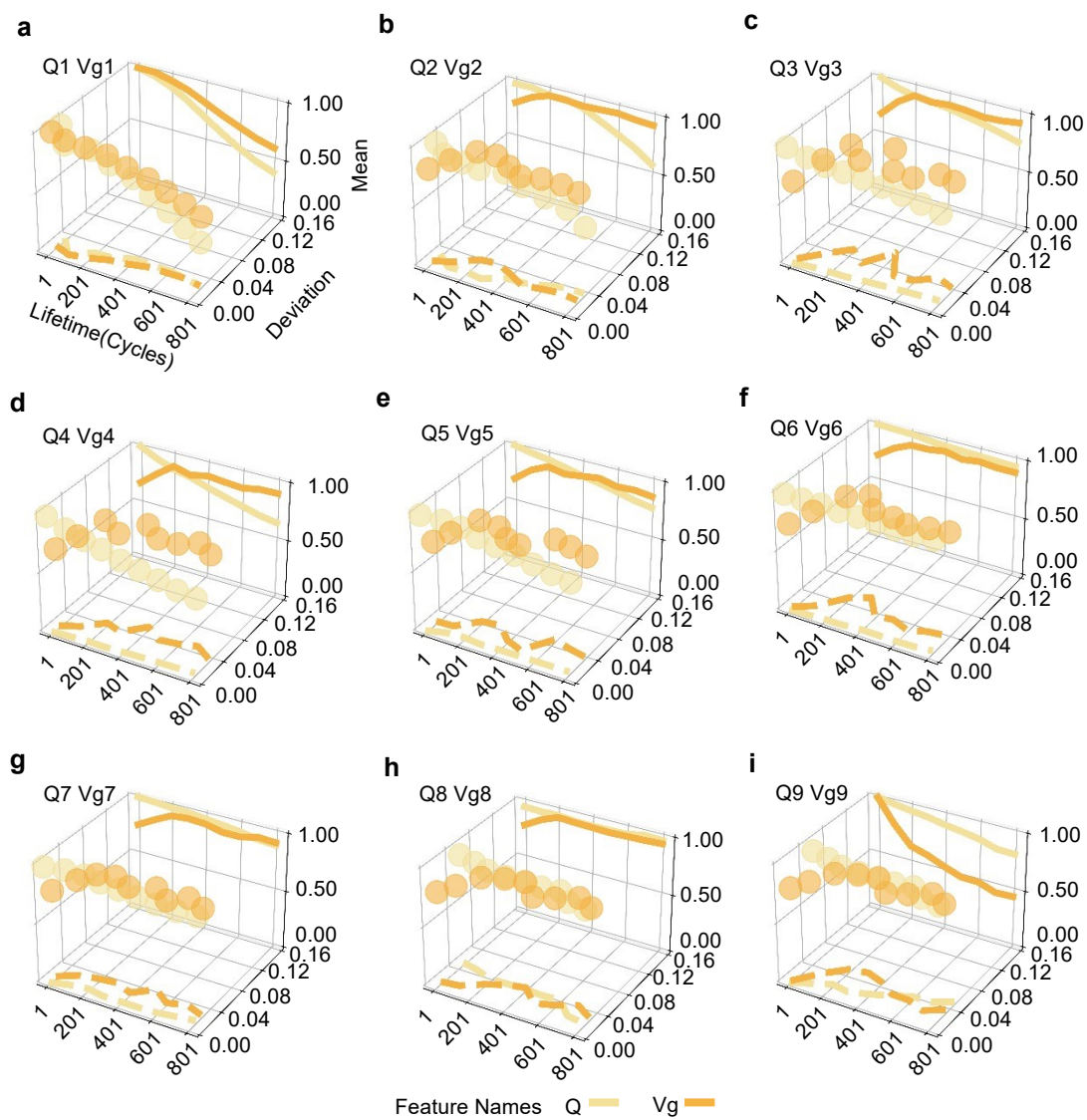
Supplementary Figure 22

The charging capacity (Q), polarization speed (Vg), and their stabilities (battery-wise standard deviation) evolution in lifetime direction for each charging stage at 55℃, respectively. (a-i) are for Q and Vg in each charging step, respectively.
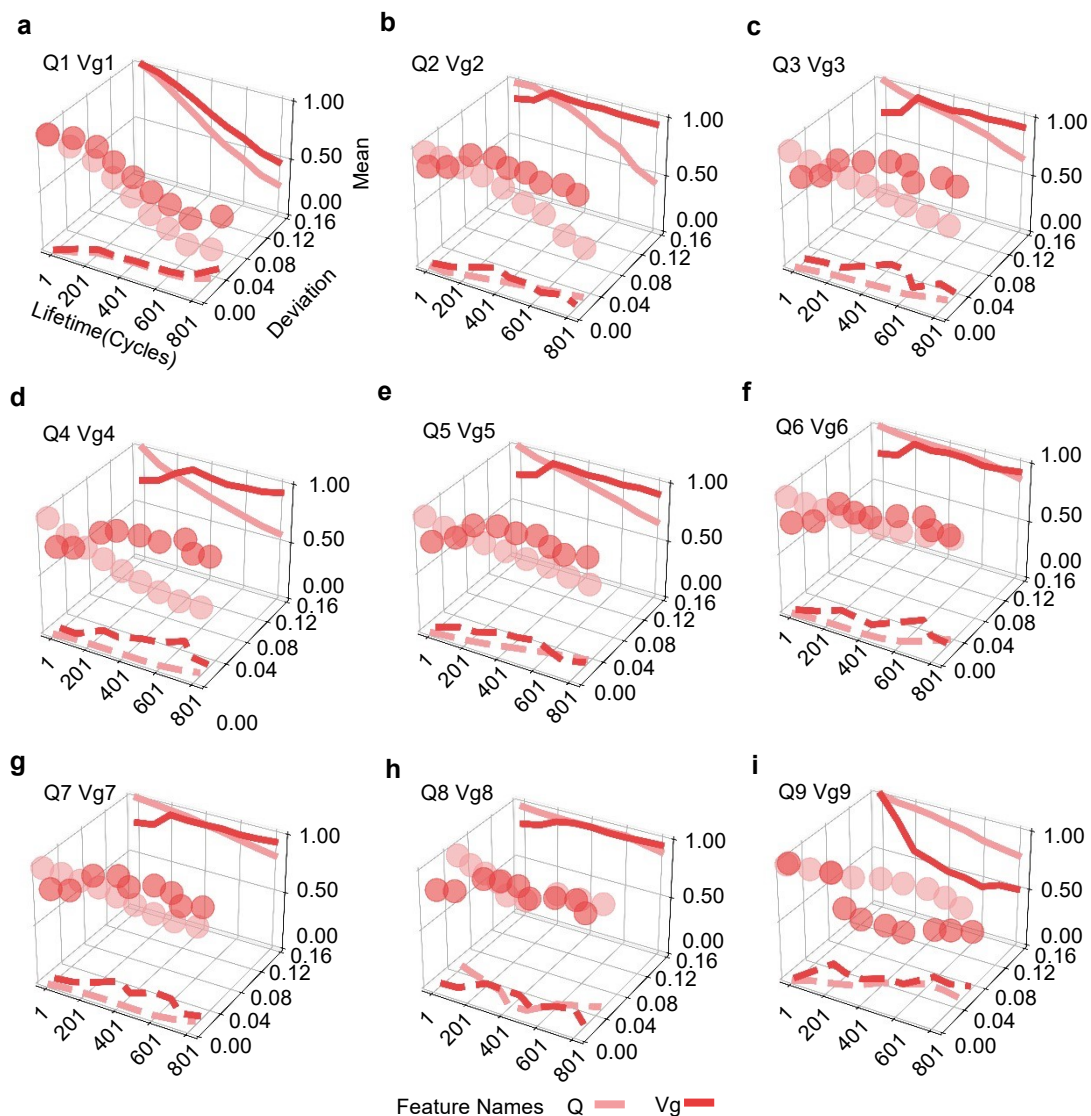
Supplementary Figure 23

Machine learning pipeline design of the physics machine learning for early prototype verification. The source domain model is trained with accessible samples by projecting the initial manufacturing variabilities (IIMVs) to multi-dimensional chemical processes. The aging rate (r_{source}) is calculated and then transferred to the target domain using the Arrhenius-inspired transferability metric. Chemical processes in the target domain are iteratively updated by the previous states. Transferred chemical processes are fed into the degradation trajectory prediction model to perform verification. Note that the Figure is a general workflow, refer to Methods for detailed explanations as well as the notations.

IMVs → Model training → Chemical Process (CP) Inference → Predicted CP $\widehat{F}_{source}$ → r_{source}

$$AT_{score}^{source \to target} = \frac{r_{target}}{r_{source}} = e^{\left(-\frac{E_a^s}{k_B T_s} + \frac{E_a^t}{k_B T_t}\right)}$$

Transferability Metric (AT_{score})

$$r_{target} = \sum_{i=1}^{K} W_i \cdot AT_{score}^{source\ i \to target} \cdot r_{source}^i$$

r_{target} → Degradation Chain → Transferred CP (F_{target}) Iteration → Model training → $\widehat{D}$ → Predicted Degradation Trajectory → Verification result

- Source domain model (accessible sample)
- Degradation-informed transfer (Arrhenius)
- Target domain model (early data/novel sample)

Supplementary Figure 24

The difference in battery degradation in early cycles (the first 200 cycles).
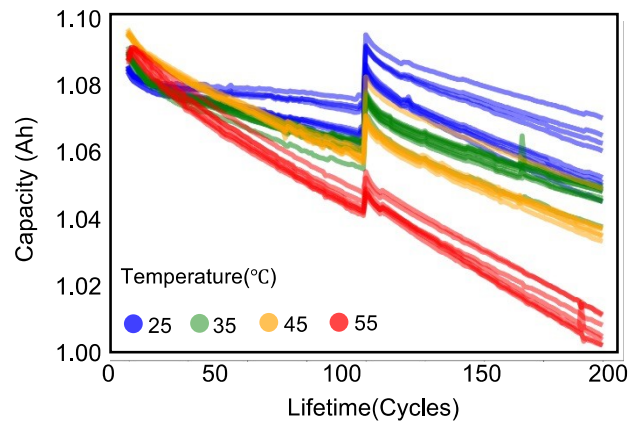
Supplementary Figure 25

The coupled relationship battery capacity loss types, degradation modes, and their correlation with underlying side reactions. Loss types can be classified into thermodynamic and kinetic loss types. Thermodynamic loss can be related to loss of active material (LAM), such as LAM at the cathode, LAM at the anode, and loss of lithium inventory (LLI). Kinetic loss can be related to impedance increment. The degradation mode and side reactions are highly coupled due to interplays between cathode particle cracking, cathode-electrolyte interphase (CEI) film formation, transition metal dissolution, electrolyte consumption, solid electrolyte interphase (SEI) film thinking, and lithium plating.
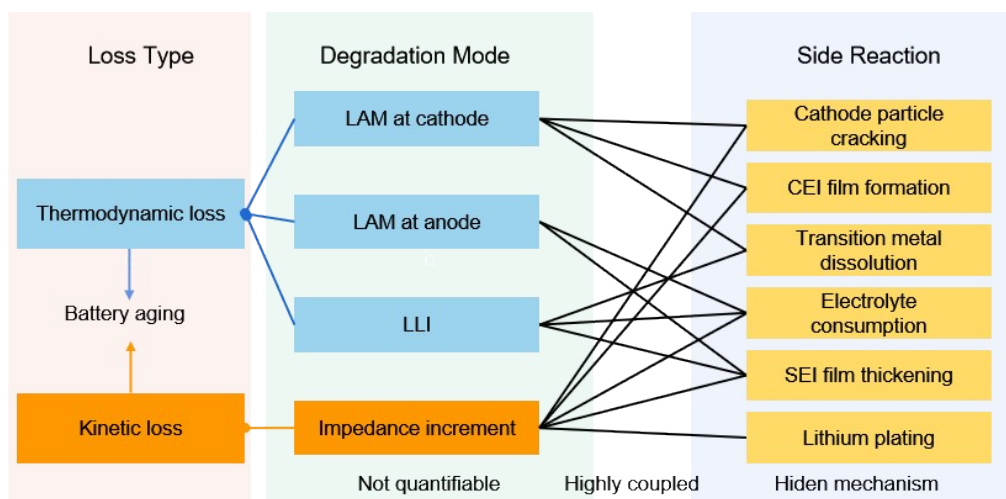
Supplementary Figure 26

Transmission electron microscopy (TEM) for characterizing the cathode-electrolyte interphase (CEI) morphology on the surfaces of two NCM811 cathodes after cycling, indicating one of the side reactions in Supplementary Figure 24. The formation of CEI consumes active materials, manifesting thermodynamic loss, and a thicker, uneven CEI layer leads to non-uniform and slowed lithium transport across the electrolyte-cathode interface, which in turn increases battery polarization, thereby demonstrating kinetic loss.
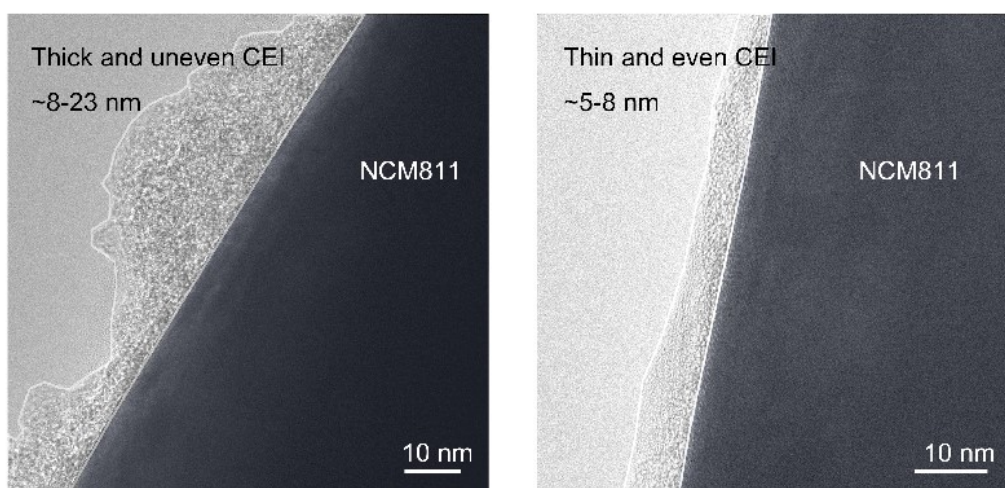
Supplementary Figure 27

Scanning electron microscopy (SEM) for characterizing surface morphology change of NCM811 particles after several cycles, indicating the cathode particle cracking in Supplementary Figure 24. The formation of cracks in cathode originates from the fragmentation of active material particles, constituting a thermodynamic loss in itself. Furthermore, the presence of cracks leads to a decline in local lithium-ion transport performance and a reduction in reaction dynamics, signifying kinetic loss. Concurrently, cracks lead to localized stress concentrations, thus continued propagation of cracks, eventually culminating in the failure of the entire particle.
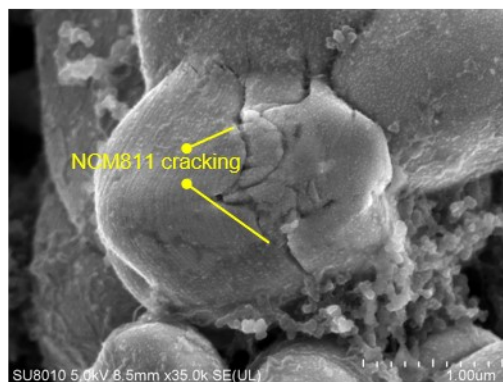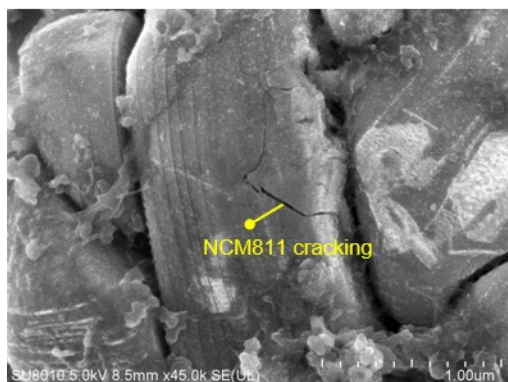
Supplementary Figure 28

Scanning electron microscopy (SEM) for characterizing the morphological changes of the graphite anode at the (a) initial state and (b) after cycles. Noticeable graphite exfoliation and the presence of lithium plating on the surface of the graphite anode can be discerned, indicating potential side reactions in Supplementary Figure 24. These two side reactions represent common failure modes for graphite anodes; exfoliation of graphite results in degradation both thermodynamically and kinetically, whereas lithium plating primarily affects kinetic loss.

Initial state   After cycles
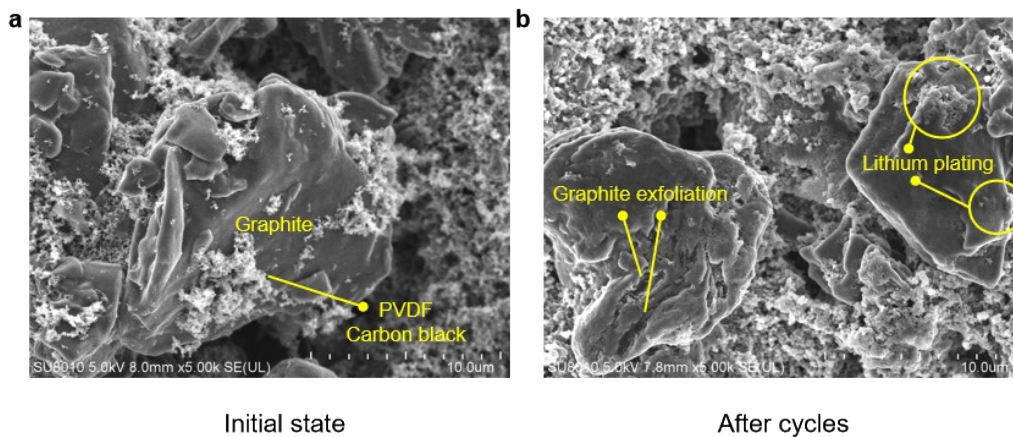
Supplementary Figure 29

The electrochemical impedance spectroscopy (EIS) results of NCM811 full cells at the (a) initial state and (b) after cycling, show an increase in the electrolyte bulk impedance (in the low-frequency region) and a slight decrease in the interface impedance (in the capacity loop) between the electrode and electrolyte interface. Note that the R, C, and W refer to the resistance, capacitance, and Warburg components, respectively. The EIS testing is commonly used in characterizing impedance increase in Supplementary Figure 24, while inaccessible in practical use cases, especially when the time efficiency is demanding.

Initial state   After cycles
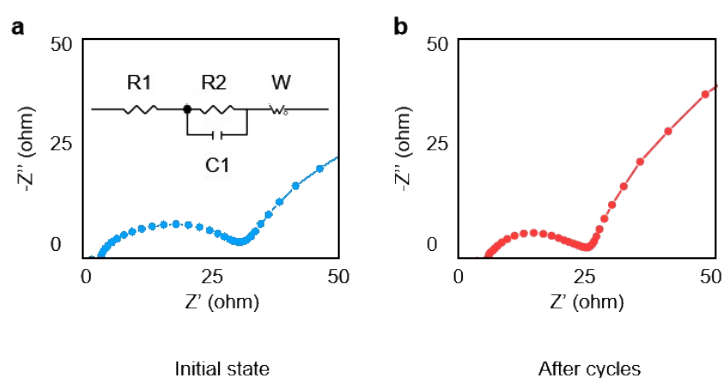
Supplementary Figure 30

Lithium-ion concentration distribution evolution inside the battery after every step from S1 to S9. It can be seen that after stages S2-6 there is a pronounced concentration polarization, reflecting the characteristics of the kinetics. Note that the notation S refers to each charging step in the multi-step charging process.
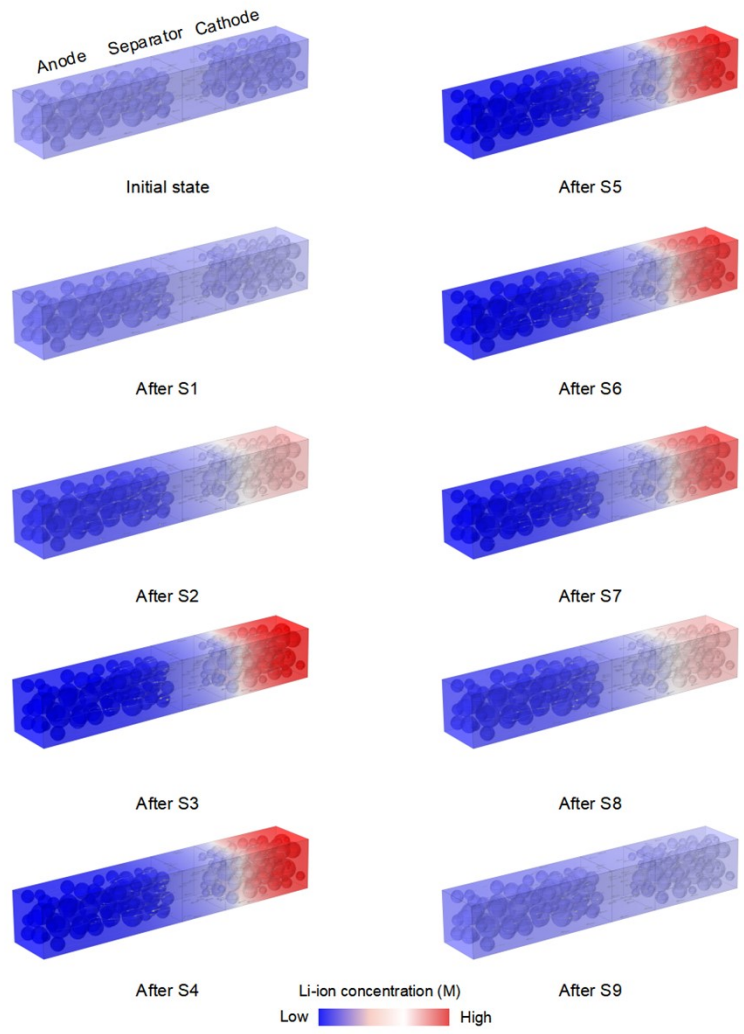
Supplementary Figure 31

Lithiation state visualization inside the anode graphite particles after every step from S1 to S9. Note that the notation S refers to each charging step in the multi-step charging process.
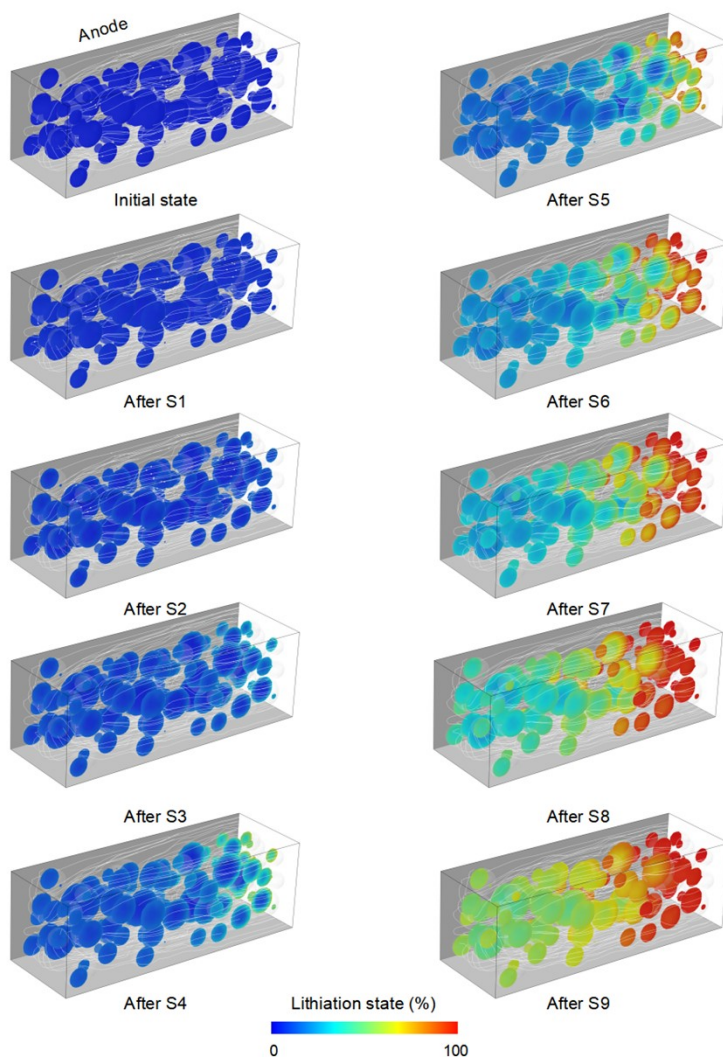
Supplementary Figure 32

Lithiation state visualization inside the cathode NCM811 particles after every step from S1 to S9. Note that the notation S refers to each charging step in the multi-step charging process.
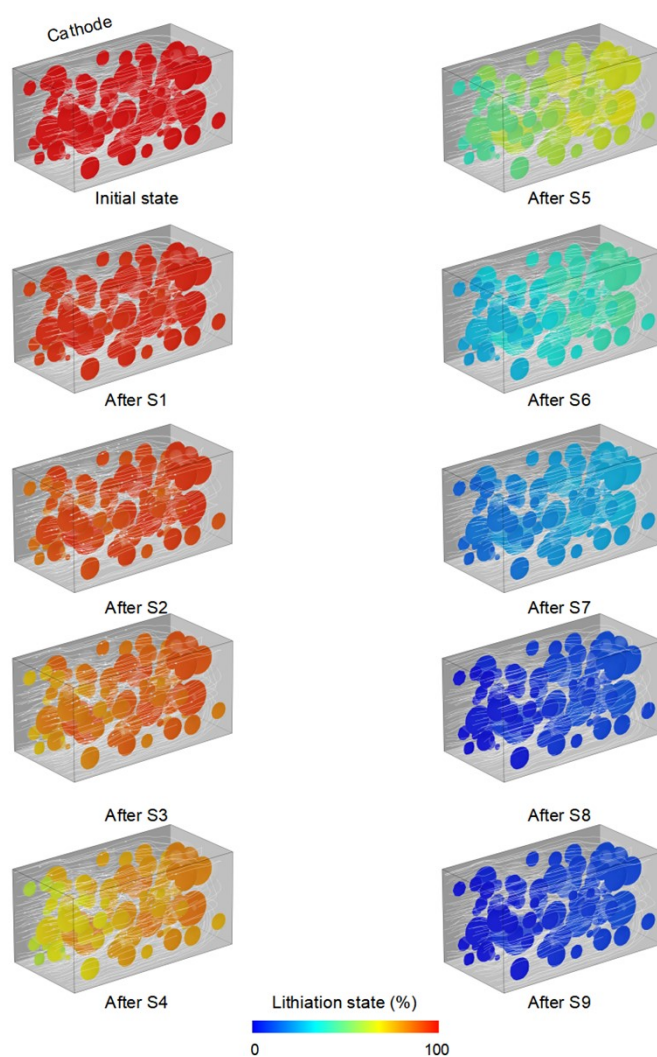
Supplementary Figure 33

The increase of SEI thickness and decrease of area activeness from the initial cycle to the 1000th cycle. The SEI thickening corresponds to LLI as thermodynamic loss, consequentially contributing to increased battery impedance, reflecting kinetic loss.
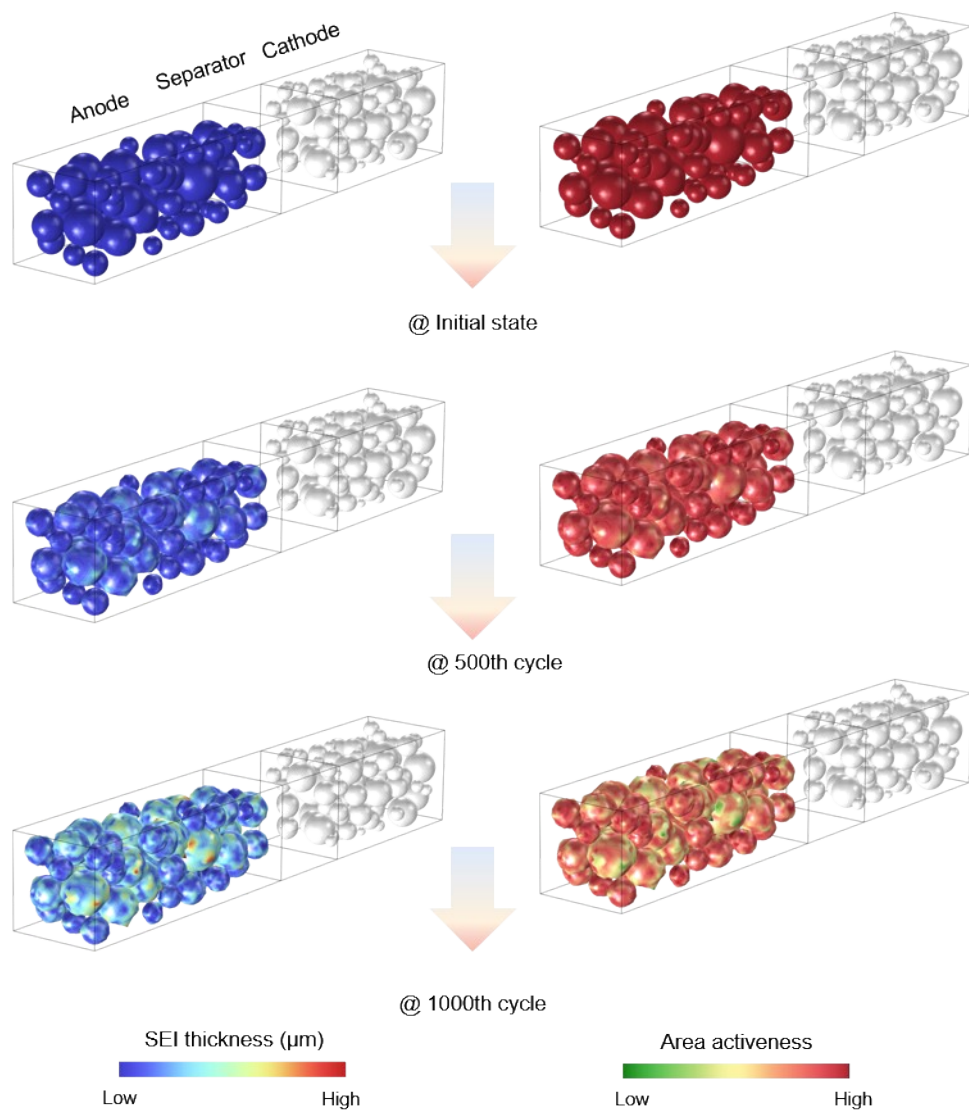
Supplementary Figure 34

The relationship between multi-step charging scheme and voltage response sensitivity in different state of charge (SOC) regions. (a) Differential voltage-capacity (dV/dQ) response to the equilibrium potential of NCM811/graphite battery, (b) multi-step charging profile, where the intra-step and inter-step between the high and low current charging stages encapsulate rich information.
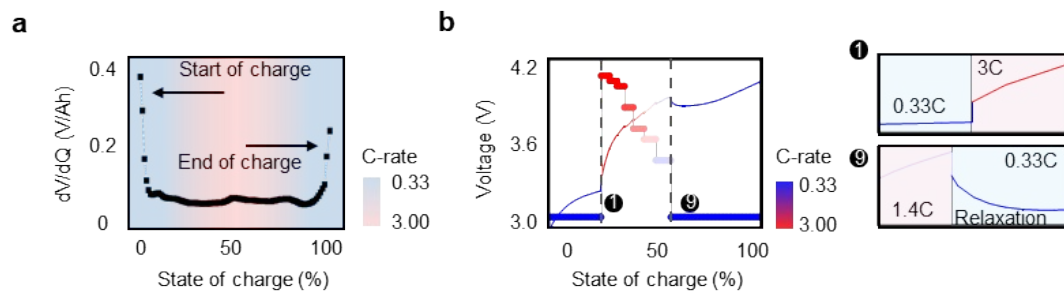
Supplementary Figure 35

The feature importance in different lifetime stages, i.e., the early, middle, and late 10% cycles of the entire lifetime under 25°C. Colorbar maps the cycle value in different stages, respectively. Zero importance is indicated with dashed lines, respectively.
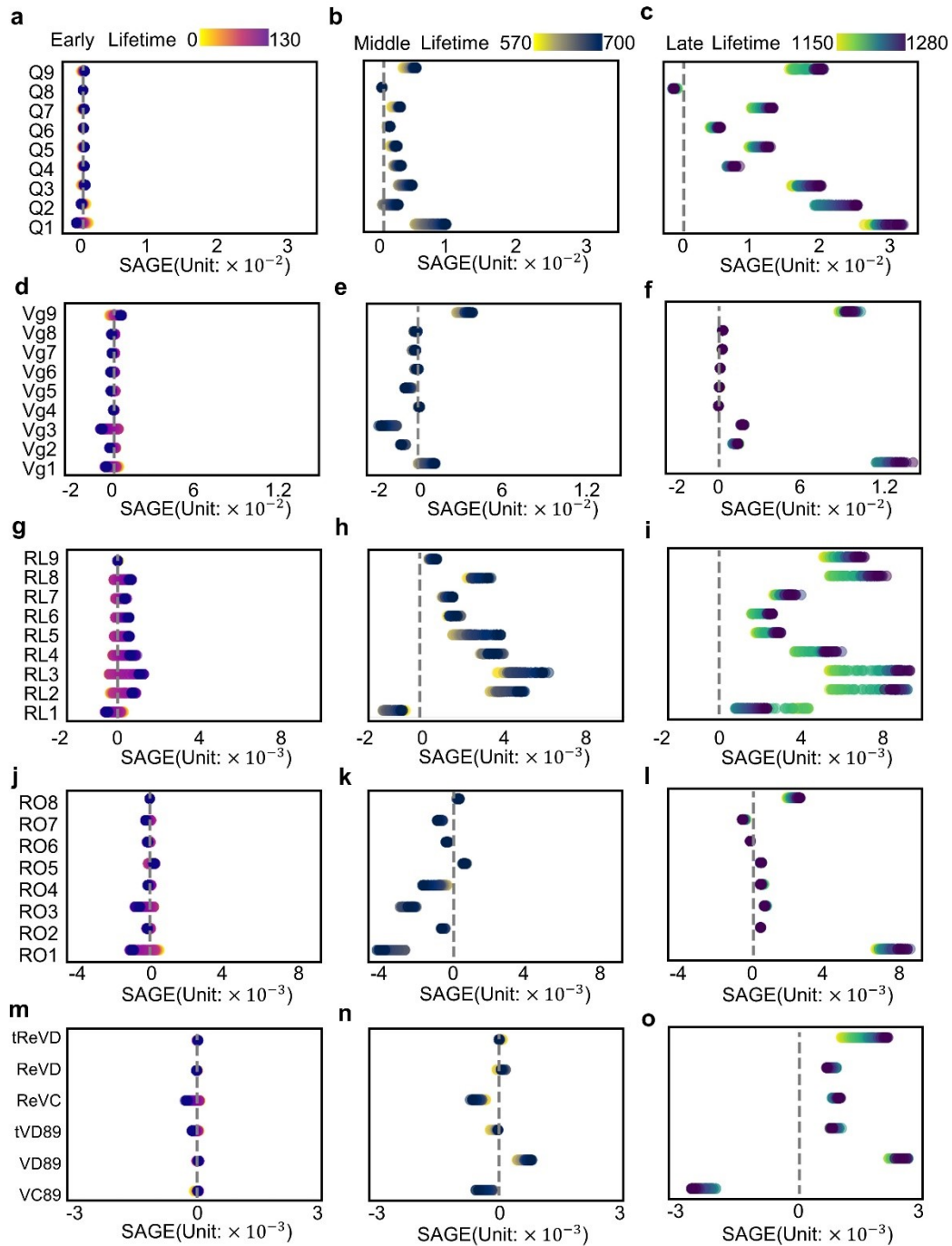
Supplementary Figure 36

The feature importance in different lifetime stages, i.e., the early, middle, and late 10% cycles of the entire lifetime under $35^\circ C$. Colorbar maps the cycle value in different stages, respectively. Zero importance is indicated with dashed lines, respectively.
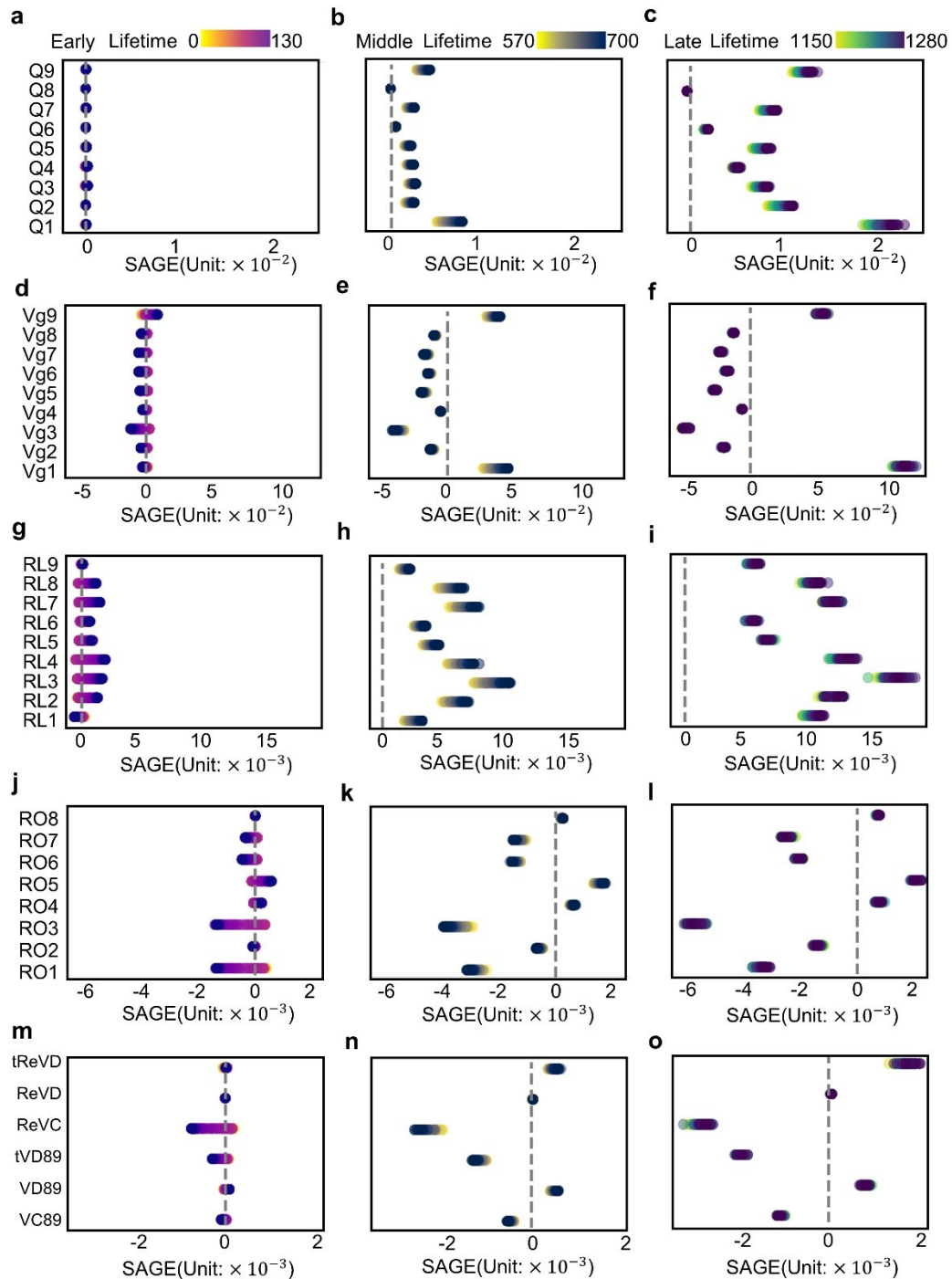
Supplementary Figure 37

The feature importance in different lifetime stages, i.e., the early, middle, and late 10% cycles of the entire lifetime under 45℃. Colorbar maps the cycle value in different stages, respectively. Zero importance is indicated with dashed lines, respectively.
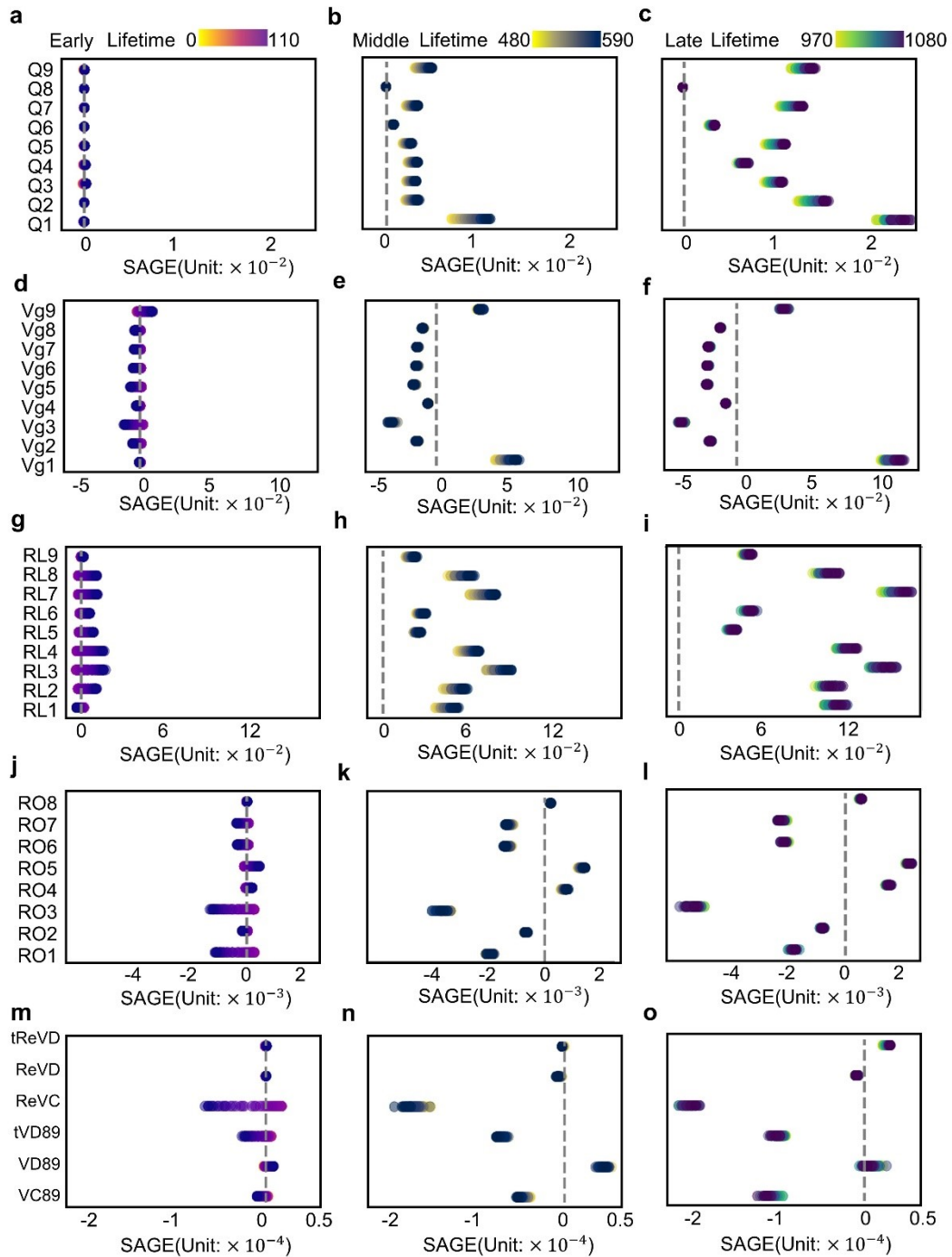
Supplementary Figure 38

The feature importance in different lifetime stages, i.e., the early, middle, and late 10% cycles of the entire lifetime under 55℃. Colorbar maps the cycle value in different stages, respectively. Zero importance is indicated with dashed lines, respectively.
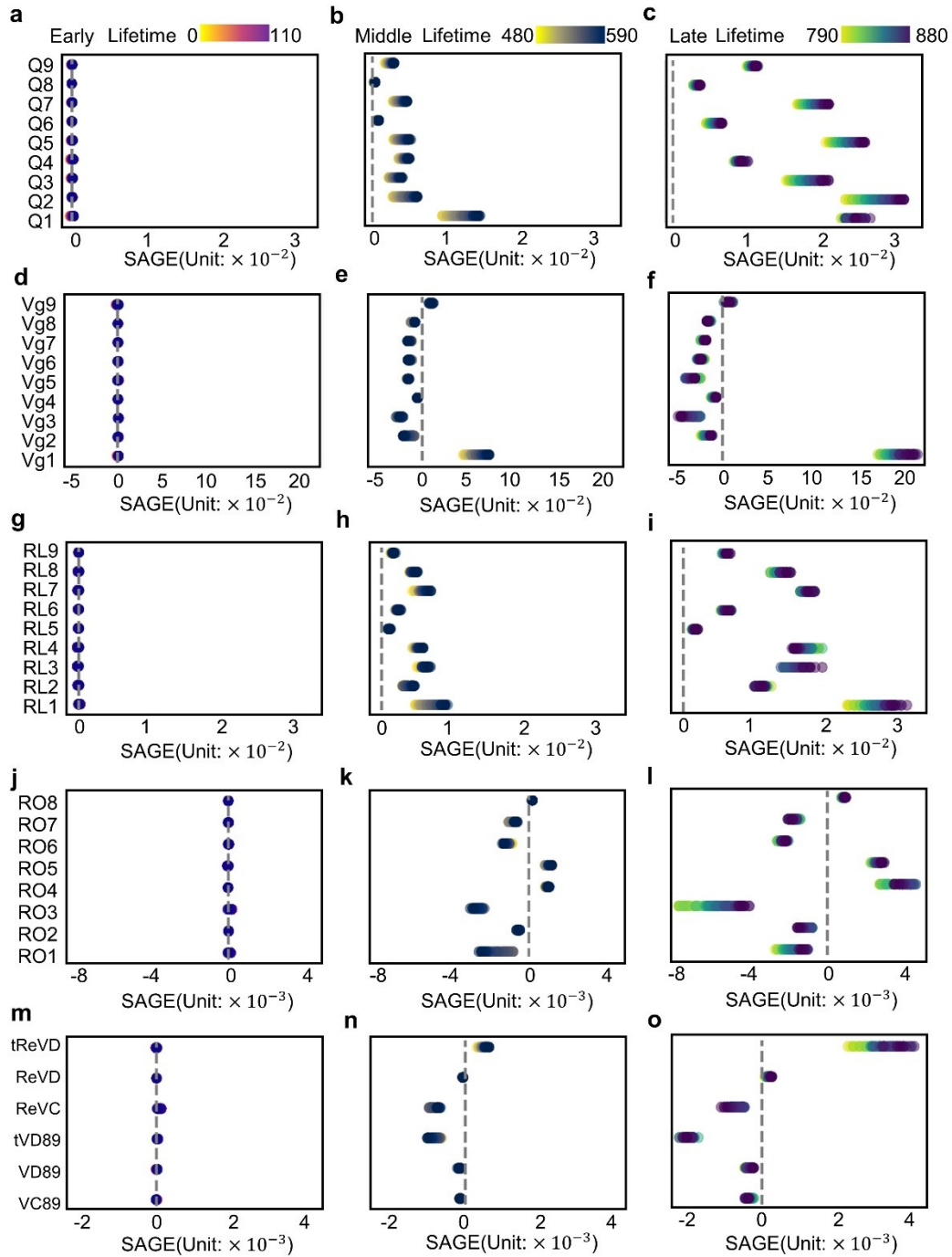
Supplementary Figure 39

The incremental capacity analysis of selected batteries at 25, 35, 45, and 55 °C, from (a) to (d), respectively. Lifetime segments, i.e., 1 to 100 and 700 to 900 are analyzed to show the dQ/dV variation in the battery lifetime direction. Loss of active material (LAM) and loss of lithium inventory (LLI) in the low state of charge regions are indicated by the shrunk peak intensity (solid arrow) and shift of peak (dashed arrow), respectively. The discharging voltage and capacity data are smoothed by a mean value moving window with a length of 20 to ensure the stability of the derivative calculations.
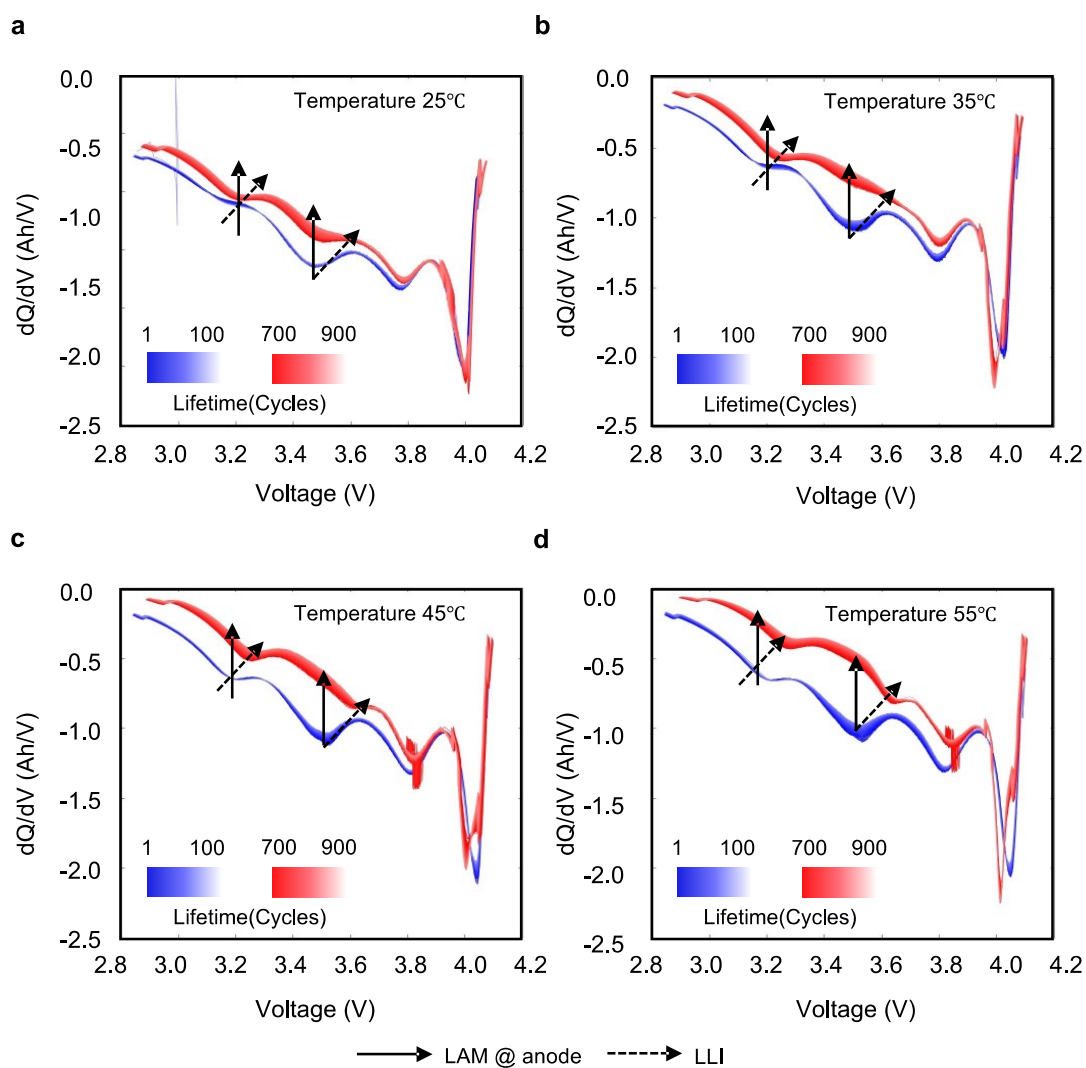
Supplementary Figure 40

Decoupled loss type, i.e., thermodynamic, and kinetic losses from total loss from simulation.
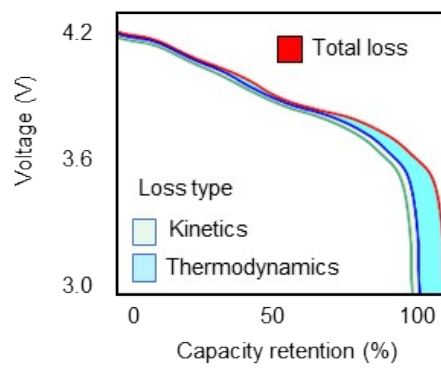
Supplementary Table 1

The design of the multi-step charging scheme. The original intention of the 9-step charging design is to optimize the battery charging strategy and achieve fast charging while reducing lithium-ion deposition. First, we set a fixed state of charge (SOC) target interval for each charging step, and apply constant current (CC) at different current rates for charging. When 1-3 cycles (Steps 3 to 14) of charging are completed, the voltages (average value) when hitting each SOC interval are used as the standard for the cut-off voltage of each stage in subsequent cycles. C_{RPT} refers to the current rate as a function of updated nominal capacity after each reference performance test (RPT). For practical use, only Steps 4 to 12 (9-step) are required for data recording and featurization.

Charging details	Time duration (min)	State of Charge (SOC)
Step1: Rest	30.00	
Step2: $0.33C_{RPT}$ CC to 2.5V	-	
Step3: Rest	30.00	
Step4: $0.33C_{RPT}$ CC to U1	14.54	+8.0%
Step5: $3.00C_{RPT}$ CC to U2	2.40	+12.0%
Step6: $2.90C_{RPT}$ CC to U3	2.07	+10.0%
Step7: $2.80C_{RPT}$ CC to U4	2.14	+10.0%
Step8: $2.40C_{RPT}$ CC to U5	2.50	+10.0%
Step9: $2.00C_{RPT}$ CC to U6	3.00	+11.1%
Step10: $1.80C_{RPT}$ CC to U7	3.33	+10.0%
Step11: $1.40C_{RPT}$ CC to U8	4.29	+10.0%
Step12: $0.33C_{RPT}$ CC to U9	28.93	+15.9%
Step13: Rest	120.00	Summation: 97%
Step14: $1C_{RPT}$ CC to (U10)	56.40	-94%
Step15: Rest	60.00	
Step16: Repeat	Steps 3 to 14 are repeated 3 times. The mean values of the (U1-U9) are taken as cut-off voltages for subsequent cycling.	

Supplementary Table 2

The training error of multi-dimensional chemical processes. The error is evaluated as the root mean square error (RMSE), considering there are near-zero values after the feature normalization manipulation. RMSEs are averaged over each lifetime observation for each feature, respectively. Note that the numerical results here are for the multi-domain adaptation, i.e., actual scenarios where intermediate temperature performance should be verified, thus batteries under 25 and $55^{\circ C}$ are assumed to be available. Predictions and error calculations are for normalized feature values. See Supplementary Note 1 for the detailed featurization taxonomy and feature ID. E stands for scientific notation, for instance, 1E-01 equals 0.1.

Feature ID	Taxonomy	Name	RMSE ($25^{\circ C}$)	RMSE ($55^{\circ C}$)
11	In-cycle (inter-step)	VC89	2.62E-04	2.18E-05
12		VD9	3.10E-05	1.36E-04
13		tVD9	1.16E-05	8.90E-05
14		ReVC	1.94E-03	2.46E-05
15		ReVD	8.65E-05	2.64E-04
16		tReVD	5.43E-04	1.37E-02
17	In-cycle (intra-step)	Vg1	7.00E-05	2.03E-04
18		Vg2	6.26E-04	1.48E-05
19		Vg3	1.95E-02	2.17E-03
20		Vg4	2.55E-03	9.16E-04
21		Vg5	2.34E-03	5.10E-04
22		Vg6	1.40E-03	9.14E-04
23		Vg7	4.65E-03	1.62E-04
24		Vg8	2.65E-03	5.35E-05
25		Vg9	3.50E-04	7.03E-04
26	In-cycle (inter-step)	RVg	7.20E-05	2.92E-03
27	In-cycle (intra-step)	Q1	9.24E-05	7.39E-04
28		Q2	1.18E-03	7.86E-04
29		Q3	5.77E-04	9.83E-04
30		Q4	1.06E-05	8.25E-05
31		Q5	2.04E-05	2.10E-05
32		Q6	1.69E-04	2.69E-03
33		Q7	1.60E-04	5.36E-05
34		Q8	5.17E-05	5.23E-03
35		Q9	2.93E-04	3.78E-05
36	In-cycle (intra-step)	RL1	2.23E-03	2.50E-04
37		RL2	1.19E-03	1.89E-04
38		RL3	1.18E-02	9.68E-04
39		RL4	2.85E-03	1.31E-03
40		RL5	7.35E-04	2.17E-04
41		RL6	4.73E-04	6.67E-04
42		RL7	2.38E-03	3.94E-04
43		RL8	3.29E-04	1.72E-04
44		RL9	9.58E-06	9.14E-05
45	In-cycle (inter-step)	RO1	2.36E-03	2.43E-04
46		RO2	2.14E-02	4.69E-04
47		RO3	3.54E-03	2.48E-03
48		RO4	3.84E-03	6.13E-04
49		RO5	3.39E-03	2.10E-03
50		RO6	6.00E-03	2.27E-04
51		RO7	5.95E-03	7.29E-05
52		RO8	6.52E-05	1.74E-04

Supplementary Table 3

The prediction error of multi-dimensional chemical processes. The error is evaluated as the root mean square error (RMSE), considering there are near-zero values after the feature normalization manipulation. RMSEs are averaged over each lifetime observation for each feature, respectively. Note that the numerical results here are for the multi-domain adaptation, i.e., actual scenarios where intermediate temperature performance should be verified, thus batteries under 35 and 45℃ are assumed to be unavailable (to be predicted rather than physical measurements). Predictions and error calculations are for normalized feature values. See Supplementary Note 1 for the detailed featurization taxonomy and ID. E stands for scientific notation, for instance, 1E-01 equals 0.1.

Feature ID	Taxonomy	Name	RMSE (35℃)	RMSE (45℃)
11	In-cycle (inter-step)	VC89	2.13E-03	1.45E-02
12		VD9	2.30E-03	2.29E-04
13		tVD9	1.11E-02	1.87E-01
14		ReVC	7.58E-04	2.04E-03
15		ReVD	3.52E-04	2.67E-06
16		tReVD	1.74E-02	9.15E-01
17	In-cycle (intra-step)	Vg1	1.09E-03	2.83E-02
18		Vg2	2.35E-03	3.72E-03
19		Vg3	1.36E-01	4.03E-02
20		Vg4	1.06E-01	3.86E-02
21		Vg5	4.06E-02	3.42E-03
22		Vg6	7.83E-02	6.50E-03
23		Vg7	3.79E-01	2.27E-02
24		Vg8	2.12E-02	1.23E-02
25		Vg9	1.17E-02	5.40E-03
26	In-cycle (inter-step)	RVg	4.29E-04	1.77E-03
27	In-cycle (intra-step)	Q1	1.68E-03	1.77E-04
28		Q2	2.91E-03	5.40E-03
29		Q3	1.01E-03	8.29E-04
30		Q4	5.33E-03	2.96E-02
31		Q5	1.62E-03	6.56E-02
32		Q6	6.81E-04	1.05E-01
33		Q7	1.59E-04	8.13E-03
34		Q8	1.82E-02	4.86E-02
35		Q9	1.46E-03	5.74E-05
36	In-cycle (intra-step)	RL1	7.27E-03	5.56E-02
37		RL2	1.65E-02	1.09E-02
38		RL3	3.32E-02	1.24E-02
39		RL4	8.42E-02	1.21E-03
40		RL5	3.20E-02	1.36E-03
41		RL6	1.27E-02	1.85E-04
42		RL7	1.83E-02	1.91E-03
43		RL8	3.72E-03	4.39E-04
44		RL9	2.89E-05	1.52E-03
45	In-cycle (inter-step)	RO1	1.12E-03	1.01E-03
46		RO2	6.07E-02	3.35E-02
47		RO3	7.37E-02	9.43E-03
48		RO4	1.18E-01	3.09E-03
49		RO5	1.26E-01	2.19E-02
50		RO6	1.10E-01	1.52E-02
51		RO7	1.79E-01	2.90E-02
52		RO8	4.02E-04	1.35E-02

Supplementary Table 4

Model early verification performance comparison when guiding samples from 55°C are available. The MAPE and STD refer to the averaged mean absolute percentage error and standard deviation across batteries at 25, 35, and 45°C. The maxMAPE refers to the maximum MAPE at a selected temperature. Model 1 is a long-short-term memory neural network model. Model 2 is our physics-informed machine learning framework without considering initial manufacturing variability. Model 3 is our physics-informed machine learning framework without using Arrhenius-inspired transfer. Model 4 is an empirical formula. Model details are in Supplementary Note 3, otherwise specified in the annotation of this Table.

	The first 50 cycles are accessible			The first 25 cycles are accessible		
	Verification temperature at 45					
	MAPE(%)	STD	maxMAPE(%)	MAPE(%)	STD	maxMAPE(%)
Ourwork	0.99	0.36	1.60	1.27	0.44	2.17
Model1	67.75	7.91	81.37	87.95	9.86	104.68
Model2	1.47	0.57	2.72	2.37	0.57	3.44
Model3	7.13	0.64	8.10	7.00	0.57	7.94
Model4	8.78	0.52	9.63	8.83	0.52	9.70
	Verification temperature at 35					
	MAPE(%)	STD	maxMAPE(%)	MAPE(%)	STD	maxMAPE(%)
Ourwork	2.11	0.73	3.37	2.52	0.80	3.68
Model1	87.99	14.68	107.38	89.78	11.76	107.01
Model2	2.54	0.19	3.57	2.60	0.19	3.80
Model3	11.56	0.59	11.97	11.04	0.79	11.44
Model4	15.66	0.72	16.69	15.89	0.78	17.10
	Verification temperature at 25					
	MAPE(%)	STD	maxMAPE(%)	MAPE(%)	STD	maxMAPE(%)
Ourwork	2.64	0.82	3.50	3.14	0.85	4.18
Model1	73.66	21.18	108.56	78.94	25.21	138.87
Model2	3.69	0.64	4.79	2.84	0.63	3.87
Model3	9.51	0.91	13.41	11.78	0.82	12.76
Model4	16.83	0.53	17.58	17.22	0.53	18.02

Supplementary Table 5

Early verification model by feature selection, i.e., thermodynamic and kinetic loss features. We use Q1+Q9 and Q2 to present thermodynamic and kinetic loss, respectively. The experimental setting is the single-source domain adaptation (only guiding samples from 55℃ are available). 200 cycles of early data from the target domain are used.

	MAPE(%)		
Verification temperature	25℃	35℃	45℃
Thermodynamic loss(Q1+Q9)	11.05	3.59	3.27
Kinetic loss(Q2)	5.32	1.10	1.12

Supplementary Table 6

The experiments showcase the dualistic challenges of prediction capability and adaptability. Exp is short for the experiment. Exp 1-4 are to verify the prediction capability when no temperature transfer is considered. Note that Exp 1-4 are toy problems for model interpretation only, thus data in non-early cycles can be used, i.e., 80% for training and 20% for testing. Exp 5-8 are to demonstrate the necessity of the joint consideration of prediction capability and adaptability. Experimental settings for Exp 5-8 are single-source domain adaptation (only guiding samples from 55°C are available). 200 cycles of early data from the target domain are used.

	MAPE(%)			
Verification temperature	25°C	35°C	45°C	55°C
Exp 1 (Q1)	0.43	0.29	0.47	0.67
Exp 2 (Q2)	0.44	0.39	0.48	0.68
Exp 3 (Vg1)	0.50	0.37	0.39	0.73
Exp 4 (Vg2)	1.02	0.62	0.83	0.93
Exp 5 (Q1)	2.70	1.35	1.88	-
Exp 6 (Q2)	2.65	1.11	0.91	-
Exp 7 (Vg1)	4.70	1.53	1.88	-
Exp 8 (Vg2)	2.84	1.60	1.55	-

Supplementary Note 1

This Supplementary Note elucidates the relationship between voltage loss, and capacity loss by demonstrating the principle of how we decouple the underlying mechanisms of capacity fade from macroscopic electric signals. We Note that the mechanism is agnostic to the cathode material types, thus being favorable of the next-generation R&D where diversities of materials are involved. During the aging process, batteries undergo internal environment alterations, such as structural changes or loss of active materials and the progression of diverse polarizations, finally leading to voltage loss. This results in the observed fact that charging voltages exceed the theoretical level, whereas discharge shows the converse effect. Due to the inherent stability window limitations of battery components, cut-off voltage values for charge and discharge are imposed, respectively. Voltage loss prompts premature attainment of these cut-off voltage values, consequently giving rise to capacity loss. Thus, voltage loss and capacity fade are directly interconnected, thereby decoupling measurable voltage signal loss presents an effective way to decouple capacity degradation.

Despite multifaceted and coupled underlying mechanisms contributing to battery degradation, the following cathode material agnostic formula can be employed to decouple voltage loss, i.e., voltage difference, between the actual electrode voltage and theoretical voltage:

$$|U_{actual} - U_{theoretical}(*)| = \Delta E(SOC,SOH,T) + \eta(I,SOC,SOH,T)$$

U_{actual} is the actual working electrode voltage. $U_{theoretical}$ is the theoretical open-circuit voltage reflective of the essential characteristics of the battery material as-manufactured prototypes, denoted by the $*$ notation. The ΔE is the thermodynamic voltage loss, attributed to the intrinsic material change due to aging, as a function of SOC, SOH, and environmental temperature T. η is the current-induced polarization, which can be further subclassified into three parts, e.g., activation polarization (η_{act}), ohmic polarization (η_{ohm}), and concentration polarization (η_{con}) as follows:

$$\eta = \eta_{act} + \eta_{ohm} + \eta_{con}$$

This material agnostic formula quantifies the respective contributions of thermodynamic and kinetic losses to the overall battery degradation, with their relative proportions changing as a function of SOC, SOH, environmental temperature T, and applied current I. Particularly, applied current causes the battery working voltage to deviate from its OCV and cannot change the

properties of materials, thus solely influencing η. In comparison, for the open-circuit state, voltage loss solely reflects thermodynamic loss contributions. As the applied current increases, kinetic loss becomes notably responsive. Therefore, by altering the applied current density, the relative proportions, equivalently the degradation pattern dominance, contributed by thermodynamic and kinetic loss can be modulated and quantified. Consequently, this seemingly simple and material-agnostic formula encapsulates nearly all factors pertinent to battery aging studies and enables *operando* decoupling of microscopic degradation mechanisms using macroscopic electric signals. Fundamentally, we use this formula as the theoretical support of our featurization taxonomy by comprehensively studying electric signals that can represent, at least the partial information of, the voltage loss. The core idea can be found in the following Figure.

$$|U_{actual} - U_{theoretical}(*)| = \Delta E(SOC, SOH, T) + \eta(\boldsymbol{I}, SOC, SOH, T)$$
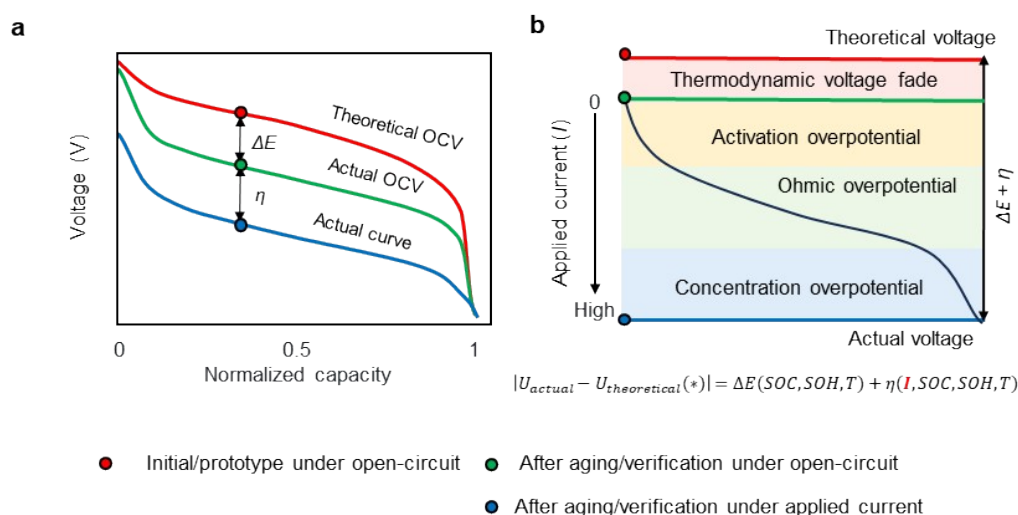
(**a**) The voltage loss between the theoretical open-circuit voltage (OCV) curve (red line, when zero current is applied, reflective of intrinsic material properties of as-manufactured prototypes) and the actual voltage curve (blue line). The difference between the lines can be divided into two major components, e.g., thermodynamic loss ΔE (reflective of the shift in intrinsic material properties when prototypes age), and kinetic loss η (current-induced polarization). The theoretical OCV plus thermodynamic loss ΔE is the actual OCV, which further plus kinetic loss η is the actual working voltage. (**b**) The η can be further categorized into three parts, e.g., activation polarization, ohmic polarization, and concentration polarization, with polarization effects (kinetic loss) becoming more pronounced as the applied current increases.

Supplementary Note 2

The feature taxonomy is designed to link statistical features to the physical meaning of chemical processes. Prior- and in-cycle features are extracted to characterize initial manufacturing variability and chemical process evolution during long-term cycling. The in-cycle features are split into inter- and intra-step features thanks to the rich dynamic information provided by multi-step charging schemes. The feature identification number, taxonomy, name, description, and physical meaning are presented in the Table below.

ID	Taxonomy	Name	Description	Physical meaning
1	-	T	Operation temperature	-
2	Prior-cycle	U1	Cut-off voltage value when assigned SOC is hit at each charging step	Charge acceptance at each charging step (SOC region) [1,2]
3		U2		
4		U3		
5		U4		
6		U5		
7		U6		
8		U7		
9		U8		
10		U9		
11	In-cycle (inter-step)	VC89	Voltage change from the end of step 8 to the start of step 9	Ohmic and electrochemical polarization, linked to SEI growth (pseudo relaxation) [3,4]
12		VD9	Voltage drop from the start of step 9 to the minimum of step 9	Concentration polarization (pseudo relaxation) [5]
13		tVD9	Time needed for VD9	Recovery time of concentration polarization (pseudo relaxation) [5]
14		ReVC	Voltage change from the end of step 9 to the start of the rest	Ohmic and electrochemical polarization, linked to SEI growth (relaxation) [3,4]
15		ReVD	Voltage drop from the start of the rest to the minimum of the rest	Concentration polarization (relaxation) [5]
16		tReVD	Time needed for ReVD	Recovery time of concentration polarization (relaxation) [5]
17	In-cycle (intra-step)	Vg1	Mean value of voltage gradient at each charging step	Polarization speed at each charging step (SOC region) [6]
18		Vg2		
19		Vg3		
20		Vg4		
21		Vg5		
22		Vg6		
23		Vg7		
24		Vg8		
25		Vg9		
Continued page				
26	In-cycle (inter-step)	RVg	Ratio of Vg2 and Vg1	
27	In-cycle (intra-step)	Q1	Charging capacity value when assigned SOC is hit at each charging step	Charge acceptance at each charging step (SOC region) [7]
28		Q2		
29		Q3		
30		Q4		
31		Q5		
32		Q6		
33		Q7		
34		Q8		
35		Q9		
36	In-cycle	RL1	Ratio of voltage and charging	Merged representation of ohmic,

37	(intra-step)	RL2	current at each charging step	electrochemical, and concentration resistance at each charging step (SOC region) [8]
38		RL3		
39		RL4		
40		RL5		
41		RL6		
42		RL7		
43		RL8		
44		RL9		
45	In-cycle (inter-step)	RO1	Ratio of voltage change and current change at switching points between steps	Ohmic resistance from relaxation behaviours [3,4]
46		RO2		
47		RO3		
48		RO4		
49		RO5		
50		RO6		
51		RO7		
52		RO8		

Supplementary Note 3

This Supplementary Note elucidates the mathematical calculation of the features in arbitrary cycles. Here we only use one cycle for demonstration of feature extraction.

For cut-off voltage features in the prior-cycling stage:

$$U_i = V(soc = soc_i)$$

$$soc_i = \{8, 20, 30, 40, 50, 61.1, 71.1, 81.1, 97\} \times 100\%$$

where, $i = \{1,2,..,9\}$, V is battery voltage, soc is the state of charge, and soc_i is the accumulated state of charge at the ith charging step.

For inter-step voltage transient features and pseudo relaxation features in the in-cycling stage:

$$VC89 = V_9(start) - V_8(end)$$

where, V_9 and V_8 are the voltage vector in the ninth and eighth charging stage, respectively. $start$ and end stand for the first and last voltage values in the vector, respectively.

$$VD9 = V_9(start) - min(V_9)$$

where, V_9 is the voltage vector in the ninth charging stage. min is the minimum operator.

$$tVD9 = t(V = V_9(start)) - t(V = min(V_9))$$

where, V_9 is the voltage vector in the ninth charging stage, min is the minimum operator, t is time and V is the battery voltage.

For inter-step relaxation features in the in-cycling stage:

$$ReVC = V_9(end) - V_{re}(start)$$

where, V_9 and V_{re} are the voltage vectors in the ninth charging stage rest stage, respectively. $start$ and end stand for the first and last voltage values in the vector, respectively.

$$ReVD = V_{re}(start) - min(V_{re})$$

where, V_{re} is the voltage vector in the rest stage. min is the minimum operator.

$$tReVD = t(V = V_{re}(start)) - t(V = min(V_{re}))$$

where, V_{re} is the voltage vector in the rest stage. min is the minimum operator. t is time and V is the battery voltage. For better time-sensitivities, $min(V_{re})$ is taken when the 80% of the maximum voltage drop is hit.

For intra-step voltage gradient features in the in-cycling stage:

$$Vg_i = mean(G(V_i))$$

where, $i = \{1,2,..,9\}$, V_i is the voltage vector at the ith charging step, G is the gradient operator and $mean$ is the mean operator.

For intra-step capacity features in the in-cycling stage:

$$Q_i = Q(soc = soc_i)$$

$$soc_i = \{8, 20, 30, 40, 50, 61.1, 71.1, 81.1, 97\} \times 100\%$$

where, $i = \{1,2,..,9\}$, Q is battery charging capacity, soc is the state of charge, and soc_i is the accumulated state of charge at the ith charging step.

For lumped resistance features in the in-cycling stage:

$$RL_i = \frac{V_i(end) - V_i(start)}{I_i}$$

where, $i = \{1,2,..,9\}$, V_i and I_i are the voltage vector and current value at the ith charging step, respectively. $start$ and end stand for the first and last voltage values in the vector, respectively.

For ohmic resistance features in the in-cycling stage:

$$RO_i = \frac{V_{i+1}(start) - V_i(end)}{I_{i+1} - I_i}$$

where, $i = \{1,2,..,8\}$, V_i and I_i are the voltage vector and current value at the ith charging step, respectively. $start$ and end stand for the first and last voltage values in the vector, respectively.

Supplementary Note 4

This Supplementary Note explains the detailed settings of benchmarking models.

Model 1 (LSTM):

Model 1 is established to examine challenges in the long-term prediction capability of our physics-informed machine learning strategy, incorporating knowledge fusion using guiding samples and early data of batteries to be verified. In Model 1, we transform the 42-dimensional features, i.e., feature ID from 11 to 52 (Supplementary Note 1), into time series data with a time step of 10, which means we use a sliding window with a length of 10 to predict the next capacity point iteratively. We use data from early cycles, i.e., the first 200 cycles to predict the later cycles. For the implementation details, we use a single-layer LSTM, MSE loss, and Adam optimizer. The training epoch is set to 50, and the batch size is set to 32 for a converged loss curve for limited early data (the loss is already converged in 30 epochs).

Model 2 (No-IMV):

Model 2 is established to examine the usefulness of probed initial manufacturing variability (IIMVs). In Model 2, we do not change the machine learning pipeline as described in the Methods section. We only remove the IIMVs from the feature matrix when performing physics-informed machine learning, i.e., the temperature transfer experiment. Therefore, the model learns from extracted features, as well as their temperature divergence, disregarding the IIMVs of the batteries. The model is expected to underperform as compared with those that include IIMVs, given the evidenced fact that IIMVs influence battery capacity during long-term cycling. The remaining settings are identical to that of the Methods sections.

Model 3 (No-transfer):

Model 3 is established to verify the necessity of physics-informed machine learning for knowledge transfer regarding different degradation patterns under continuous temperature regions. In Model 3, the physics-informed machine learning, i.e., the Arrhenius law is not adopted thus the verification of target samples can only access the source sample information, regardless of the evidenced feature divergence under different temperatures. The model is expected to underperform compared with those that include a physics-informed machine learning strategy,

since temperature adaptation is a necessity. The remaining settings are identical to that of the Methods sections.

Model 4 (Empirical formula):

Model 4 is established to verify the necessity of automatic temperature calibration of models as opposed to expert knowledge in a fixed temperature, which is typically not accessible in battery prototype verification as prior knowledge. In Model 4, as a common engineering practice to save test time, we use polynomial fitting to determine an empirical formula that is suitable for batteries at hand, for instance, guiding samples. The obtained empirical formula is a mapping from the cycle index to the capacity values at a fixed temperature. For verification, such empirical formula is calibrated using the distance matching between early data of batteries to be verified and guiding samples. The distance matching is implemented by a translation transformation, where the translation is an intercept shift determined by the averaged capacity differences of early data at different temperatures. Such an empirical formula makes it hard to characterize the temperature-induced degradation patterns. The cycle index of batteries to be verified is fed into the calibrated empirical formula to get the capacity values. The model is expected to underperform and is not robust since it heavily relies on the temperature variation of battery performance (which is not prior) and involves no chemical process evolution insights.

Supplementary Note 5

We have demonstrated the dualistic challenges of early validation of battery prototypes due to a combination of prediction capability and transferability performance [7]. Therefore, we are motivated to find features that have both prediction capability and transferability performance. On one hand, the kinetic processes taking into account the influence of temperature shift are expressed by the high-current phase of our taxonomy framework. We need to find out features expressing dynamics that have better prediction capability. On the other hand, taking into account thermodynamic processes that are not affected by temperature and are expressed by the characteristics of the small current phase of our taxonomy framework, we need to find features expressing thermodynamics that have better transferability performance. Note that both prediction capability and transferability are not independent of each other, we interpret transferability (experiments designed with domain adaptation) by analyzing the relative reduction of the verification error with the identical feature input. For instance, when evaluating the transferability of feature A, we first evaluate the single domain prediction error, noted e_1; we then evaluate the domain adaption prediction error, noted e_2. We take the $e = |e_1 - e_2|$ as an evaluation metric. The smaller e, the better the transferability of the feature. Prediction capability is evaluated by e_1. The smaller e_1, the better the prediction capability of the feature.

Supplementary Note 6

Here we show the method to determine the actual variation of chemical processes, which can be categorized as the characterization techniques, electrochemical testing methods, and sensing techniques:

Visualizing the battery's microscopic degradation mechanisms heavily relies on advanced and expensive characterization techniques. For instance, X-ray diffraction (XRD) is employed to analyze changes in crystal structures of battery materials [9], such as phase transitions in cathode and anode. Scanning electron microscopy (SEM) and transmission electron microscopy (TEM) enable observation of the morphological changes in electrodes during charge-discharge cycles, particularly concerning the morphology and thickness of the CEI/SEI layer and particle cracking [10]. X-ray photoelectron spectroscopy (XPS) [11] and Fourier-transform infrared spectroscopy (FTIR) [12] are used to examine surface chemical compositions and bond changes in battery materials, which are instrumental in studying the chemical makeup of SEI/CEI layers and the impact of electrolyte decomposition products on capacity fade. Nuclear magnetic resonance (NMR) [13] and Raman spectroscopy [14] offer insights into local structural and chemical environment changes for battery components, etc. However, despite lots of available characterization techniques, they often provide only partial glimpses into the complex degradation mechanisms. To truly visualize and disentangle the intricate aging mechanisms inside batteries, there remains a pressing need to develop even more sophisticated *in-situ* characterization techniques.

Electrochemical testing methods also play a significant role in analyzing the microscopic processes associated with battery capacity fade. Techniques like cyclic voltammetry (CV), electrochemical impedance spectroscopy (EIS) [15], differential capacity/voltage curves, and relaxation tests allow non-destructive monitoring of the evolution of internal resistance in batteries over cycles and SOC. CV primarily serves to investigate the reversibility and activity of electrochemical kinetic within batteries over specific potential ranges [16]. In degradation mechanism studies, as cycle number increases, structural change in active materials or growth of the SEI layer may lead to changes in the CV curve, such as diminution of peak currents, emergence of new peaks, or shifts in peak positions [17]. EIS aids in elucidating the complex charge transfer and mass transport processes within the battery. During battery aging, the EIS spectra can reveal characteristic impedance changes that reflect microscopic mechanisms, such as electrode

material cracking, increased SEI/CEI film thickness, and electrolyte depletion. Relaxation testing can delve into the dynamic processes occurring within the battery, including the diffusion rate of Li-ions within the electrode materials and electrolytes. However, these electrochemical testing methods often require specialized testing instruments, and cannot directly correspond to the underlying microscopic mechanisms. The interpretation of measurements demands substantial expertise and supplementary characterization approaches, and the decoupling of these curves is also very dependent on the precise definition of the initial model.

In addition, certain battery sensors play a crucial role in characterizing critical parameters of battery performance, such as voltage, current, temperature, internal resistance, and physical changes that may impact the SOH and SOC. However, integrating these sensors often requires corresponding data analysis algorithms and it should be noted that many sensors are invasive to the battery, not easily portable for installation, necessitate complex methods to decouple sensor signals, and incur associated costs [18].

Given the numerous challenges in characterizing battery aging status using the aforementioned methods, there is an urgent need to develop an easy-to-integrate and non-invasive intelligent algorithm capable of discerning the *in-situ* internal electrochemical information through the disentanglement of macroscopic battery profiles.

Supplementary Note 7

We visualized the evolution of various physical fields within the battery during the multi-step charging process as well as throughout the battery degradation cycle. The software environment is the Comsol Multiphysics 6.1 platform. The entire simulation process consists of two procedures: the first step focuses on the reproduction of the multi-step charging process, and the second step is modeling the capacity fade of the battery, informed by degradation insights provided by machine learning. In the simulation of the multi-step charging process, we first determined the cut-off voltage according to the real charging condition, see Supplementary Table 1, and used it as the cut-off voltage for the subsequent charging and discharging process. In the simulation of the battery aging process, according to insights gained from machine learning, the dominant contribution to battery capacity loss is thermodynamic loss, while the polarization contributing to kinetic loss is primarily driven by concentration polarization. Therefore, our simulation involves modeling the formation of SEI on the anode, along with consumption of electrolyte and LLI due to SEI formation which represents the thermodynamic loss, concurrently contributing to increased battery impedance, reflecting kinetic loss. By adjusting the stoichiometric coefficient of LLI in the side reaction of SEI generation and the conductivity after SEI generation, we achieve control of the proportion of thermodynamic and kinetic loss, respectively. Simultaneously, the thickening of the SEI layer and the consumption of the electrolyte inherently affect the concentration polarization in the battery, thus aligning with the insights derived from machine learning. We established two sets of models, the three-dimensional model to qualitatively visualize the state of each physical quantity inside the battery, and the one-dimensional numerical model to quantitatively analyze the capacity loss.

The first part is about the basic charge transfer and mass transport processes in the battery.

Based on the pseudo-two-dimensional model framework for battery simulations [19,20], the following are the principal governing equations:

In the electrolyte, the transport of ions is governed by the Nernst−Planck equation:

$$N_i = -D_{e,i}\left(\nabla c_{e,i} - \frac{z_i F c_{e,i}}{RT}\nabla\Phi\right) \#(1)$$

where, N_i is flux, $D_{e,i}$, z_i and $c_{e,i}$ is the diffusion coefficient in the electrolyte, charge and concentration of species i, respectively. F is the Faraday's constant, R is the ideal gas constant, T is the Kelvin temperature and Φ is the electrolyte potential.

The ions present within the electrolyte adhere to the principles of both mass conservation and charge conservation, which can be represented as:

$$\frac{\partial c_{e,i}}{\partial t} + \nabla \times N_i = 0 \#(2)$$

$$\sum_i z_i c_{e,i} = 0 \#(3)$$

where, z_i is the valence of each species in the electrolyte.

At the interface of the electrolyte and the electrode, the electron transfer between Li^+ and Li atoms can be expressed by the following simplified reaction:

$$Li^+ + e^- \leftrightarrow Li \#(4)$$
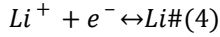
This reaction could be quantified by the Butler-Volmer equation:

$$i_{loc} = i_{ex}\left[\exp\left(\frac{\alpha_a F \eta}{RT}\right) - \exp\left(\frac{-\alpha_c F \eta}{RT}\right)\right]\#(5)$$

where, i_{loc} is the local current density, which could be used to quantify the local reaction rate. η is overpotential, α_a and α_c are the anodic and cathodic charge transfer coefficients, respectively, and i_{ex} is exchange current density.

The overpotential can be calculated as:

$$\eta = \phi_s - \phi_e - U_{eq} \#(6)$$

where, ϕ_s and ϕ_l is the solid phase and liquid phase potential, respectively, U_{eq} is the equilibrium potential of the reaction.

In the cathode/anode particles, Li atoms diffuse into/out the inner/outer particles due to the concentration gradient, and could be expressed by the Fick's second law:

$$\frac{\partial c_s}{\partial t} = D_s\left(\frac{\partial^2 c_s}{\partial r^2} + \frac{2\partial c_s}{r \partial r}\right)\#(7)$$

where, D_s is the diffusion coefficient of Li atoms in the cathode particles, r is the radius of the particle, c_s is the Li atom concentration.

The open-circuit potential U of NCM811 and graphite particles can be calculated according to the Nernst equation:

$$U = U_{eq} + \frac{RT}{nF}ln\left(\frac{c_{e,Li}}{c_s}\right)\#(8)$$

where, n is the number of electrons transferred.

The second part is about the simulation details of the aging process.

We choose to consider the growth of the SEI on the anode for simulating the battery aging process [21,22], and in addition to the primary graphite lithium intercalation reactions occurring on the anode, we also analyze the following side reaction:

$$S + nLi^+ + ne^- \rightarrow P_{SEI} \#(9)$$
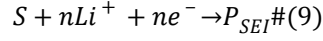
where, S represents the solvent, P_{SEI} denotes the products formed during the reaction, and n is the number of lithium ions consumed. The generation of P_{SEI} leads to the loss of lithium inventory within the battery, causing an increase in the resistance of the SEI, as well as a decrease in the electrolyte volume fraction within the graphite anode.

The kinetics of this side reaction can be expressed by:

$$i_{loc,SEI} = -(1 + HK)\frac{i_{loc}}{\exp\left(\frac{\alpha_a F \eta}{RT}\right) + \frac{q_{SEI} f J}{i_{loc}}} \#(10)$$

where, i_{loc} is the local current density as mentioned above, HK is a dimensionless number representing the graphite expansion factor, which depends on the graphite's state of charge. HK is zero during the lithiation process. J is a dimensionless number representing the exchange current density for parasitic reactions. q_{SEI} signifies the local cumulative charge caused by the formation of the SEI. f is a lumped dimensionless parameter based on the properties of the SEI film.

The concentration c_{SEI} of SEI can be used to calculate the SEI thickness as follows:

$$\frac{\partial c_{SEI}}{\partial t} = -\frac{\gamma_{SEI} i_{loc,SEI}}{nF} \#(11)$$

where, γ_{SEI} is the stoichiometric coefficient of SEI.

The q_{SEI} above is directly proportional to the c_{SEI}:

$$q_{SEI} = -\frac{F c_{SEI}}{A_v} \#(12)$$

where A_v is the area of the electrode surface.

Then the thickness of SEI layer δ_{SEI} can be calculated:

$$\delta_{SEI} = -\frac{M_P c_{SEI}}{A_v \rho_P} \#(13)$$

where, M_P and ρ_P are the molar mass and density of SEI, respectively.

Generally, it takes multiple cycles for a battery to exhibit noticeable capacity loss, hence it is often assumed that the incremental differences between each cycle during cycling are very small. In our

model, each simulated charge-discharge cycle is considered to represent the average aging characteristics over a large number of actual cycles τ. Moreover, assuming that all lithium captured in the SEI layer after a full charge-discharge cycle can be attributed to the anode, the accelerated capacity loss can be represented by re-writing the stoichiometry of the SEI formation reaction as follows:

$$(\tau - 1)S + n(\tau - 1)Li \rightarrow (\tau - 1)P_{SEI} \#(14)$$
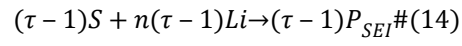
Combining with the equation (9), we can get:

$$\tau S + nLi^+ + n(\tau - 1)Li \rightarrow \tau P_{SEI} \#(15)$$
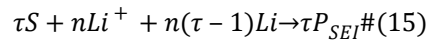
Supplementary Note 8

Here we show the method to determine the statistical contribution of loss types using Shapley values [23] and benchmarking degradation values. All features describing loss types are interpreted by our featurization taxonomy to depict certain physical meanings. Statistical contribution is determined by the feature importance calculation from the multi-source domain adaptation model, i.e., 25 and 55 ℃, to obtain a general insight into intermediate temperature regions. 200 cycles of early data from 35 and 45 ℃ are fed into the machine learning model to learn the statistical contribution of loss types. Note that full features are fed into the machine learning model. See the Methods section for a detailed calculation of the statistical feature importance.

Statistical contribution of loss types:

For thermodynamic loss and kinetic loss, small current stages define a dominated thermodynamic loss, while large current stages define a dominated kinetic loss. For thermodynamic loss, we use the summation of the absolute value of feature importance for Q1 and Q9 as the thermodynamic loss contribution to the overall capacity loss. For the kinetic loss, we use the summation of the absolute value of feature importance for Q2, Q3, Q4, Q5, Q6, Q7, and Q8 as the kinetic loss contribution to the overall capacity loss. For concentration polarization and other polarization types, VC89 stands for ohmic and electrochemical polarization, while VD stands for concentration polarization. For both loss type and polarization, the statistical contribution is defined as the physical contribution of the loss type. For instance, when the mean absolute importance of Q1 and Q9 is 4 (a.u.) while the mean absolute importance of Q2, Q3, Q4, Q5, Q6, Q7, and Q8 is 1 (a.u.), the physical contribution of thermodynamic and kinetic loss is 80% and 20%, respectively.

Benchmarking degradation values:

The benchmarking degradation values are defined as the true degradation quantities of selected features. Before calculating benchmarking degradation values, original values are normalized to the region of zero to one. For selected features, we take the absolute value of the difference between the feature value at the first and the 800th cycle, respectively. This absolute difference is the quantified feature degradation in the context of the selected feature. For instance, when the absolute difference of Q1 at the first and the 800th cycle is 0.2 (a.u.), we take the thermodynamic loss represented by Q1 as 0.2 (a.u.), which is regarded as the truth by manipulating the raw data.
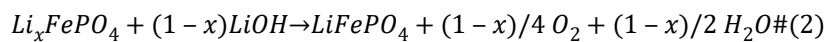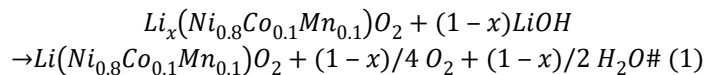
Note that the features with the same physical meaning in featurization taxonomy can be linearly combined.

Supplementary Note 9

Here we present the techno-economic assessment methodology of four battery recycling methods, i.e., refined direct, direct, hydrometallurgy, and pyrometallurgy recycling, each differentiated by their process and efficiency. The methodology begins by assessing the SOH of the prototype battery, leading to a detailed comparison of the recycling methods by decomposing the physical material treatment processes and quantifying their associated input-output relationship.
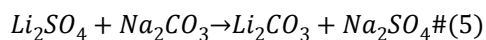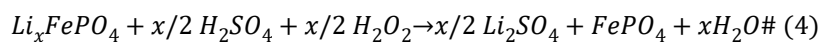
The refined direct recycling method is highlighted for its efficiency, avoiding the need to dismantle the battery structure. We note that such efficiency is enabled by our non-destructive characterization method using machine learning-inspired degradation pattern insights. This approach utilizes Lithium naphthalenide (Li-Naph) as a supplementary lithium source, directly enhancing the battery capacity without the need for preprocessing steps. The method significantly lowers costs related to materials, labor, and equipment by skipping the dismantling phase, showcasing its potential for efficient recovery of cells[24].

Contrastingly, the remaining conventional recycling methods still require extensive preprocessing, including disassembly, separation, and a blend of chemical and physical treatments. Initially, these processes involve shredding the cells into powder and removing non-recyclable battery components, yielding a 'black mass' rich in valuable materials like lithium, nickel, and cobalt. The subsequent steps differ among the methods, with some emphasizing converting the black mass into metallic salts, while others aim to rejuvenate the cathode active materials via structural repair.

The direct recycling employs lithium hydroxide as a supplementary lithium source, employing specific chemical reactions to restore the active cathode materials for both NMC811 and LFP cells, respectively:

$$Li_x(Ni_{0.8}Co_{0.1}Mn_{0.1})O_2 + (1-x)LiOH$$
$$\rightarrow Li(Ni_{0.8}Co_{0.1}Mn_{0.1})O_2 + (1-x)/4\ O_2 + (1-x)/2\ H_2O \# (1)$$

$$Li_xFePO_4 + (1-x)LiOH \rightarrow LiFePO_4 + (1-x)/4\ O_2 + (1-x)/2\ H_2O \#(2)$$

The hydrometallurgy recycling involves leaching active materials into solvents using sulfuric acid and hydrogen peroxide, extracting and precipitating critical metals like nickel, cobalt, and manganese as sulfates, and using soda ash to recover lithium carbonate:

$$Li_x(Ni_{0.8}Co_{0.1}Mn_{0.1})O_2 + (x + 2)/2\ H_2SO_4 + (2 - x)/2\ H_2O_2$$
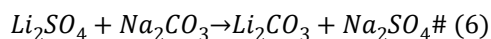$$\rightarrow x/2\ Li_2SO_4 + (2 - x)/2\ O_2 + 0.8NiSO_4 + 0.1CoSO_4 + 0.1MnSO_4 + 2H_2O\#\ (3)$$

$$Li_xFePO_4 + x/2\ H_2SO_4 + x/2\ H_2O_2 \rightarrow x/2\ Li_2SO_4 + FePO_4 + xH_2O\#\ (4)$$

$$Li_2SO_4 + Na_2CO_3 \rightarrow Li_2CO_3 + Na_2SO_4\#(5)$$
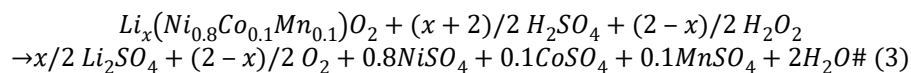
The pyrometallurgy recycling incinerates the black mass to obtain a matte of nickel and cobalt, from which lithium is eventually recovered as carbonate:

$$Li_2SO_4 + Na_2CO_3 \rightarrow Li_2CO_3 + Na_2SO_4\#\ (6)$$

The technology-economic assessment methodology incorporates detailed data encompassing the composition of feedstock by weight percentage, the fate and rates of components, and equipment parameters across various recycling processes. It further includes the economic and environmental aspects by detailing the prices of consumed and recovered materials, alongside cost information specific to recycling practices in China.

Here we detail the feedstock composition of different recycling methods. It is delineated by weight percentage, component fate, and recovery rates. The data is presented in the Table below. Given the assumption that cells are encased in aluminum shells, materials such as iron or steel are not considered in the composition. The pyrometallurgy and hydrometallurgy recycling methods, aim to transform black mass into lithium carbonate, nickel sulfate, cobalt sulfate, and manganese sulfate, each achieving different recovery rates. Conversely, methods like refined direct recycling and direct recycling aim to restore the active cathode materials directly. The associated data was sourced from the EverBatt model, an open-source model developed by Argonne National Laboratory, which evaluates recycling costs and environmental impacts[25].

Table The feedstock composition of different recycling methods

Refined direct recycling			
	LFP	NMC811	Fate and recovery rates
Defective Cells	100%	100%	100% recovery
Preprocessing			
	LFP	NMC811	Fate and efficiency
Cathode materials	45.7%	42.9%	95% to black mass
Graphite	22.5%	29.1%	95% to black mass
Carbon black	1.0%	0.9%	95% to black mass
Binder: PVDF	1.0%	0.9%	5% to black mass
Binder: anode	0.5%	0.6%	5% to black mass
Copper	9.6%	7.8%	90% to copper powder 5% to black mass
Aluminum	5.9%	5.2%	90% to aluminum powder 5% to black mass
Electrolyte: $LiPF_6$	1.9%	1.7%	Burn for energy

Electrolyte: EC	5.8%	5.4%	Burn for energy
Electrolyte: DMC	4.7%	4.3%	Burn for energy
Plastic: PP	1.1%	0.8%	Burn for energy
Plastic: PE	0.2%	0.2%	Burn for energy
Plastic: PET	0.3%	0.3%	Burn for energy
Direct recycling			
	LFP	NMC811	Fate and efficiency
Cathode materials	65.2%	58.2%	90% recovery
Graphite	32.2%	39.5%	90% recovery
Carbon black	1.4%	1.2%	90% recovery
Binder: PVDF	0.1%	0.1%	Landfill after treatment
Binder: anode	0.03%	0.04%	Landfill after treatment
Copper	0.7%	0.6%	Discharge after treatment
Aluminum	0.4%	0.4%	Discharge after treatment
Hydrometallurgy recycling			
	LFP	NMC811	Fate and efficiency
Cathode materials	65.2%	58.2%	Li 95% to Li_2CO_3 Ni 99% to NiSO4 Co 99% to CoSO4 Mn 99% to $MnSO_4$
Graphite	32.2%	39.5%	90% recovery
Carbon black	1.4%	1.2%	90% recovery
Binder: PVDF	0.1%	0.1%	Landfill after treatment
Binder: anode	0.03%	0.04%	Landfill after treatment
Copper	0.7%	0.6%	Discharge after treatment
Aluminum	0.4%	0.4%	Discharge after treatment
Pyrometallurgy recycling			
	LFP	NMC811	Fate and efficiency
Cathode materials	65.2%	58.2%	Li 85% to Li_2CO_3 Ni 90% to NiSO4 Co 90% to CoSO4 Mn 90% to $MnSO_4$
Graphite	32.2%	39.5%	Burn for energy
Carbon black	1.4%	1.2%	Burn for energy
Binder: PVDF	0.1%	0.1%	Burn for energy
Binder: anode	0.03%	0.04%	Burn for energy
Copper	0.7%	0.6%	Discharge after treatment
Aluminum	0.4%	0.4%	Discharge after treatment

Here we detail the equipment parameters for the recycling methods. It is posited that the operation would handle 100,000 tonnes of rejected cells annually, operating 20 hours a day for 320 days a year. The variables such as electrical power, labor requirements, and equipment costs are subject to changes according to the volume of processed materials and the assortment of utilized machinery. Notably, the wheel loader, which runs on diesel, has its electrical power consumption listed as zero. These parameters in the Table below were also extracted from the EverBatt model[25].

Table The equipment parameters of different recycling methods

Refined direct recycling				
Equipment	Number	Electrical power (kW)	Labor requirements (person-hours/day)	Cost of equipment ($)
Conveyor	1	29.8	2	36,067

Infusion machine	1	29.8	24	8,603
Wheel loader	1	0.0	20	183,000

Preprocessing

Equipment	Number	Electrical power (kW)	Labor requirements (person-hours/day)	Cost of equipment ($)
Hopper	1	29.8	6	68,088
Conveyor	4	119.3	8	144,324
Crusher	1	149.1	6	72,061
Screen, vibrating	1	352.0	6	390,300
Heat treatment furnace	1	3897.0	12	3,363,972
Cyclone	1	149.1	6	1,749,237
Eddy current separator	1	149.1	0	411,291
Air classifier	1	149.1	6	326,822
Gas treatment	1	664.9	12	610,000
Wheel loader	1	0.0	20	183,000

Direct recycling

Equipment	Number	Electrical power (kW)	Labor requirements (person-hours/day)	Cost of equipment ($)
Conveyor	1	29.8	2	36,067
Froth flotation cell	1	29.1	6	1,116,857
Filter press	2	19.5	12	304,372
Dryer	1	1975.3	6	1,737,927
Ball mill	1	143.4	6	274,459
Heat treatment furnace	1	3893.8	12	33,521,387
Water treatment	1	666.4	12	610,000
Wheel loader	1	0.0	20	183,000

Hydrometallurgy recycling

Equipment	Number	Electrical power (kW)	Labor requirements (person-hours/day)	Cost of equipment ($)
Conveyor	1	29.8	2	36,067
Leaching tank	1	71.6	12	1,234,271
Mixing tank	1	71.6	6	1,234,271
Filter press	1	9.9	6	152,186
Solvent extraction unit	3	698.0	36	6,279,234
Evaporator	1	149.1	6	879,688
Precipitation tank	1	232.7	12	2,093,078
Centrifuge	1	149.1	6	469,813
Dryer	1	4591.1	6	2,248,876
Water treatment	1	666.4	12	610,000
Wheel loader	1	0.0	20	183,000

Pyrometallurgy recycling

Equipment	Number	Electrical power (kW)	Labor requirements (person-hours/day)	Cost of equipment ($)
Hopper	1	29.8	6	68,088
Conveyor	2	59.7	4	72,134
Smelter	1	11722.2	24	28,946,046
Gas treatment	1	666.4	12	610,000
Granulator	1	20.1	6	207,097
Leaching tank	2	3.6	24	594,248
Solvent extraction unit	3	6.7	36	891,372
Filter press	1	8.2	6	152,186
Precipitation tank	1	8.9	12	486,111
Centrifuge	1	149.1	6	469,813
Dryer	1	96.0	6	283,778
Water treatment	1	666.4	12	610,000
Wheel loader	1	0.0	20	183,000

Here we detail the material prices. The analysis includes prices for both consumed and recovered materials, considering the average prices from March 20, 2023, to March 20, 2024, or the latest available data up to March 20, 2024. The pricing for chemicals is adjusted to reflect their anhydrous forms or 100% concentration levels, with specific adjustments for compounds like Li-Naph, which is derived from Naphthalene[24], and divalent metal cations prices (e.g., Ni^{2+} in Ni salt/oxide) standardized to 100% concentration based on sulfate comparisons. The price for crude lithium carbonate is pegged at 50% of the battery-grade chemical price.

Table The price of consumed and recovered materials

Consumed materials		
Materials	Prices ($/kg)	Source
Defective Cells (LFP)	1.81	https://data-pro.smm.cn/
Defective Cells (NMC811)	5.44	https://data-pro.smm.cn/
Hydrogen Peroxide	0.53	https://www.100ppi.com/
Lime	0.07	https://www.100ppi.com/
Limestone	0.07	https://www.100ppi.com/
Lithium Carbonate	27.39	https://data-pro.smm.cn/
Lithium Hydroxide	47.30	https://data-pro.smm.cn/
Li-Naph	1.13	https://www.100ppi.com/
Nitrogen	0.07	https://www.100ppi.com/
Sand	0.05	https://www.100ppi.com/
Soda Ash	0.38	https://www.100ppi.com/
Sodium Hydroxide	0.49	https://www.100ppi.com/
Sulfuric Acid	0.03	https://www.100ppi.com/
Recovered materials		
Materials	Prices ($/kg)	Source
Aluminum	2.65	https://data-pro.smm.cn/
Copper	9.65	https://data-pro.smm.cn/
Co^{2+} in Co salt/oxide	24.93	https://data-pro.smm.cn/
Graphite	1.41	https://data-pro.smm.cn/
LFP powder	9.75	https://data-pro.smm.cn/
Lithium Carbonate (crude)	13.70	https://data-pro.smm.cn/
Mn^{2+} in Mn salt/oxide	2.47	https://data-pro.smm.cn/
Ni^{2+} in Ni salt/oxide	20.02	https://data-pro.smm.cn/
NMC811 powder	31.17	https://data-pro.smm.cn/
LFP cell	15.64	https://data-pro.smm.cn/
NMC811 cell	32.22	https://data-pro.smm.cn/

The recycling cost information pertinent to China was also gathered from EverBatt[25]. Adjustments were made to tailor the model to the geographic nuances of China, ensuring an accurate reflection of the recycling landscape within the region. The data is shown in the Table below.

Table The cost information for recycling in China

	Cost	Source
Direct labor ($/hour)	4.60	https://www.kanzhun.com/
Electricity cost ($/kWh)	0.10	https://d.qianzhan.com/
Natural gas cost ($/MMBTU)	16.11	https://data-pro.smm.cn/

Water cost ($/gallon)	0.002	https://d.qianzhan.com/
Wastewater discharge cost ($/gallon)	13.70	https://d.qianzhan.com/
Landfill cost ($/ton)	10.00	https://d.qianzhan.com/
Wastewater discharge ($/gallon)	13.70	https://data-pro.smm.cn/

Economic outcomes can be derived by entering the aforementioned parameters into EverBatt.

The life-cycle environmental impact and emission categories evaluated in EverBatt include total energy use, water consumption, air pollutant emissions, and greenhouse gas (GHG) emissions. The total energy use can be broken down into fossil fuel use and non-fossil fuel use, and the fossil fuel use can be further broken down into coal, natural gas, and petroleum. Air pollutant emissions modeled in EverBatt include volatile organic compound (VOC), carbon monoxide (CO), nitrogen oxides (NO_x), sulfur oxides (SOx), particulate matter with diameters of 10 micrometers and smaller (PM10), particulate matter with diameters of 2.5 micrometers and smaller (PM2.5), black carbon (BC), and organic carbon (OC). GHGs include carbon dioxide (CO_2), methane (CH_4), and nitrous oxide (N_2O). These environmental impact and emission categories are output attributes of the GREET LCA model[26].

The life-cycle environmental impacts of each process in EverBatt are calculated based on the materials and energy flows through the process, and the environmental impact intensities of each raw material and energy input obtained from the GREET model, by the following equation:

$$EI_k = \sum_i m_i \times ei_{i,k} + \sum_j q_j \times ei_{j,k} + P_k$$

Where EI_k denotes the life-cycle environmental impact/emission category k for the process (for clarity's sake, let's assume the environmental impact/emission category k is GHG emissions hereinafter, but it could be any of the environmental impact/emission categories listed above); m_i denotes the mass (in kg) of material i consumed in the process; $ei_{i,k}$ denotes the GHG emissions for 1kg of material i in GREET; q_j denotes the quantity (in MJ) of energy type j consumed in the process; $ei_{j,k}$ denotes the GHG emissions for 1 MJ of energy type j in GREET; and P_k denotes GHG emissions from the process as a result of combustion or thermal decomposition of the raw materials (e.g., combustion of graphite in the pyrometallurgical recycling process, thermal decomposition of Li_2CO_3 in the NMC cathode powder production process).

Supplementary Note 10

Here we adopt the Transport Impact Model (TIM) to forecast the amount of rejected (defective) manufacturing-stage lithium-ion battery prototypes in China[27-29]. The TIM gathers data on lithium-ion battery installations and incorporates a range of factors to generate its forecasts. These factors include the growth of the Gross Domestic Product (GDP), the elasticity of vehicle sales, the penetration rate of electric vehicles (EVs), and technological advancements. Utilizing this approach, TIM can predict the annual production and retirement of various kinds of batteries spanning from 2020 to 2060. For the years 2023 and 2030, TIM has estimated the scrap rates to be 7.67% and 4.34% of battery production, respectively[30]. These estimates are based on an exponential function fitted to historical and projected data, providing a methodological foundation for deriving future scrap rates used in this study. Through this analysis, TIM offers valuable insights into the lifecycle of lithium-ion batteries in the Chinese market, enabling stakeholders to prepare for the future dynamics of battery recycling and disposal.

Supplementary Discussion 1

We rationalize the role of the multi-step charging profile in enabling the feature taxonomy definition framework by providing otherwise cost-intensive and time-consuming degradation measurements, such as IIMVs, thermodynamics, kinetics, and polarizations. We note that the multi-step profile is widely adopted in EV fast charging to reduce lithium plating and heat generation, but it has not been utilized for microscopic degradation quantification while undertaking a significant interpretability concern when machine learning is deployed in real-world cases. Fundamentally, we provide a data-driven characterization for microscopic degradation behaviors, such as loss and polarization types, an open-ended challenge that requires invasive sensing or characterization techniques[31,32]. Noted that we only use accessible macroscopic electric signals, the microscopic insights are promising to reveal in a non-destructive manner, expediting the iteration speed of material R&D, concerning thermal stability regulation, lithium plating detection, charging protocol design, and production optimization, especially bringing post-lithium batteries into commercial realities[33-37].

We prospect that our findings are widely applicable for promoting the lifecycle sustainability of batteries, inclusive of prototype R&D in the manufacturing, moreover, primary applications (EVs), secondary applications (reuse), and recycling (for both in-production scrap materials and retired batteries). For EV applications, IIMVs can be extended to periodical measurements for consistency updates, distinct from the capacity-based evaluations as a cost of time and full charge-discharge cycles, which is infeasible in EV applications. The bowl-shaped IIMV distribution also suggests battery consistency, especially under fast charging conditions, is promising to be properly managed by regulating temperatures for better operational safety[38-40]. Considering that the charging process is the only controllable stage in EV operation, our feature taxonomy is hopeful of estimating the SOH, bringing special attention to the potential degradation mechanism and subsequent alert to dangerous capacity diving. Signals of interest could be extracted from partial stages when EV users leave the charging station, mitigating the need for a complete charging cycle for data curation. Such thermal and health management is accessible and reliable, without extra investments in advanced in-vehicle sensor integrations, thus being favorable to immediate onboard deployment. Retired batteries face heterogeneities, which are mainly reflected in complex

retirement conditions, such as randomly distributed historical use, cathode material types, physical formats, SOC, and SOH. The heterogeneities are major pretreatment challenges while assuming critical importance to battery reuse safety, pricing, and sustainability. Physics-inspired machine learning can obtain the internal state of the retired batteries using only electrical signals, favorable to non-invasive and plug-and-play retired battery pretreatment. For recycling, we demonstrate two-folded implications concerning not only retired batteries but also in-production scrap materials from prototypes. For manufactured prototypes, we highlight an early and accurate lifetime trajectory prediction, otherwise in trial and error, expediting microscopically informed prototype verification. Scrap materials are potentially recycled by being explicitly advised by machine learning insights of degradation mechanisms, accounting for the increasing importance of economically feasible and sustainable post-lithium battery R&D.

Supplementary References

1   Li, K., Wei, F., Tseng, K. J. & Soong, B. H. A Practical Lithium-Ion Battery Model for State of Energy and Voltage Responses Prediction Incorporating Temperature and Ageing Effects. *IEEE Transactions on Industrial Electronics* **65**, 6696-6708 (2018). https://doi.org:10.1109/TIE.2017.2779411

2   Jiang, J., Liu, Q., Zhang, C. & Zhang, W. Evaluation of Acceptable Charging Current of Power Li-Ion Batteries Based on Polarization Characteristics. *IEEE Transactions on Industrial Electronics* **61**, 6844-6851 (2014). https://doi.org:10.1109/TIE.2014.2320219

3   Messing, M., Shoa, T. & Habibi, S. Estimating battery state of health using electrochemical impedance spectroscopy and the relaxation effect. *Journal of Energy Storage* **43**, 103210 (2021). https://doi.org:https://doi.org/10.1016/j.est.2021.103210

4   Chen, Z. X. *et al.* Cathode Kinetics Evaluation in Lean-Electrolyte Lithium-Sulfur Batteries. *J Am Chem Soc* **145**, 16449-16457 (2023). https://doi.org:10.1021/jacs.3c02786

5   Zhu, J. *et al.* Data-driven capacity estimation of commercial lithium-ion batteries from voltage relaxation. *Nature Communications* **13**, 2261 (2022). https://doi.org:10.1038/s41467-022-29837-w

6   Fath, J. P. *et al.* Quantification of aging mechanisms and inhomogeneity in cycled lithium-ion cells by differential voltage analysis. *Journal of Energy Storage* **25**, 100813 (2019). https://doi.org:https://doi.org/10.1016/j.est.2019.100813

7   Tao, S. *et al.* Battery Cross-Operation-Condition Lifetime Prediction via Interpretable Feature Engineering Assisted Adaptive Machine Learning. *ACS Energy Letters* **8**, 3269-3279 (2023). https://doi.org:10.1021/acsenergylett.3c01012

8   Seo, M. *et al.* Innovative lumped-battery model for state of charge estimation of lithium-ion batteries under various ambient temperatures. *Energy* **226**, 120301 (2021). https://doi.org:https://doi.org/10.1016/j.energy.2021.120301

9   Epp, J. in *Materials Characterization Using Nondestructive Evaluation (NDE) Methods*   (eds Gerhard Hübschen, Iris Altpeter, Ralf Tschuncky, & Hans-Georg Herrmann) 81-124 (Woodhead Publishing, 2016).

10   Zaefferer, S. A critical review of orientation microscopy in SEM and TEM. *Crystal Research and Technology* **46**, 607-628 (2011). https://doi.org:https://doi.org/10.1002/crat.201100125

11   Seah, M. P. The quantitative analysis of surfaces by XPS: A review. *Surface and Interface Analysis* **2**, 222-239 (1980). https://doi.org:https://doi.org/10.1002/sia.740020607

12   Li Juntao, F. J., Su Hang, Sun Shigang. Interfacial Processes of Lithium Ion Batteries by FTIR Spectroscopy. *Progress in Chemistry* **23**, 349-356 (2011).

13   Pecher, O., Carretero-González, J., Griffith, K. J. & Grey, C. P. Materials' Methods: NMR in Battery Research. *Chemistry of Materials* **29**, 213-242 (2017). https://doi.org:10.1021/acs.chemmater.6b03183

14   Wei, Z. *et al.* Probing Li-ion concentration in an operating lithium ion battery using in situ Raman spectroscopy. *Journal of Power Sources* **449**, 227361 (2020). https://doi.org:https://doi.org/10.1016/j.jpowsour.2019.227361

15   Gaberšček, M. Understanding Li-based battery materials via electrochemical impedance spectroscopy. *Nature Communications* **12**, 6513 (2021). https://doi.org:10.1038/s41467-021-26894-5

16   Kim, T. *et al.* Applications of Voltammetry in Lithium Ion Battery Research. *J. Electrochem.*

Sci. Technol **11**, 14-25 (2020). https://doi.org:10.33961/jecst.2019.00619

17   Xie, W. *et al.* Degradation identification of LiNi0.8Co0.1Mn0.1O2/graphite lithium-ion batteries under fast charging conditions. *Electrochimica Acta* **392**, 138979 (2021). https://doi.org:https://doi.org/10.1016/j.electacta.2021.138979

18   Huang, J., Boles, S. T. & Tarascon, J.-M. Sensing as the key to battery lifetime and sustainability. *Nature Sustainability* **5**, 194-204 (2022). https://doi.org:10.1038/s41893-022-00859-y

19   Doyle, M., Fuller, T. F. & Newman, J. Modeling of Galvanostatic Charge and Discharge of the Lithium/Polymer/Insertion Cell. *Journal of The Electrochemical Society* **140**, 1526 (1993). https://doi.org:10.1149/1.2221597

20   Guo, M., Kim, G.-H. & White, R. E. A three-dimensional multi-physics model for a Li-ion battery. *Journal of Power Sources* **240**, 80-94 (2013). https://doi.org:https://doi.org/10.1016/j.jpowsour.2013.03.170

21   Ekström, H. & Lindbergh, G. A Model for Predicting Capacity Fade due to SEI Formation in a Commercial Graphite/LiFePO4 Cell. *Journal of The Electrochemical Society* **162**, A1003 (2015). https://doi.org:10.1149/2.0641506jes

22   Ning, G., White, R. E. & Popov, B. N. A generalized cycle life model of rechargeable Li-ion batteries. *Electrochimica Acta* **51**, 2012-2022 (2006). https://doi.org:https://doi.org/10.1016/j.electacta.2005.06.033

23   Chen, H., Covert, I. C., Lundberg, S. M. & Lee, S.-I. Algorithms to estimate Shapley value feature attributions. *Nature Machine Intelligence* **5**, 590-601 (2023). https://doi.org:10.1038/s42256-023-00657-x

24   Ogihara, N. *et al.* Direct capacity regeneration for spent Li-ion batteries. *Joule* (2024). https://doi.org:https://doi.org/10.1016/j.joule.2024.02.010

25   Dai, Q. *et al.* EverBatt: A closed-loop battery recycling cost and environmental impacts model. (Argonne National Lab.(ANL), Argonne, IL (United States), 2019).

26   Dai, Q., Kelly, J. C., Gaines, L. & Wang, M. Life cycle analysis of lithium-ion batteries for automotive applications. *Batteries* **5**, 48 (2019).

27   Hao, H., Geng, Y. & Sarkis, J. Carbon footprint of global passenger cars: Scenarios through 2050. *Energy* **101**, 121-131 (2016).

28   Hao, H. *et al.* Impact of transport electrification on critical metal sustainability with a focus on the heavy-duty segment. *Nature communications* **10**, 5398 (2019).

29   Hao, H., Liu, Z., Zhao, F., Li, W. & Hang, W. Scenario analysis of energy consumption and greenhouse gas emissions from China's passenger vehicles. *Energy* **91**, 151-159 (2015).

30   Yu, L., Bai, Y., Polzin, B. & Belharouak, I. " Unlocking the value of recycling scrap from Li-ion battery manufacturing.": Challenges and outlook. *Journal of Power Sources* **593**, 233955 (2024).

31   Xue, Z. *et al.* Asynchronous domain dynamics and equilibration in layered oxide battery cathode. *Nature Communications* **14**, 8394 (2023). https://doi.org:10.1038/s41467-023-44222-x

32   Yuan, X., Liu, B., Mecklenburg, M. & Li, Y. Ultrafast deposition of faceted lithium polyhedra by outpacing SEI formation. *Nature* **620**, 86-91 (2023). https://doi.org:10.1038/s41586-023-06235-w

33   Zeng, Y. *et al.* Nonintrusive thermal-wave sensor for operando quantification of degradation

in commercial batteries. *Nature Communications* **14**, 8203 (2023). https://doi.org:10.1038/s41467-023-43808-9

34   Li, Y. *et al.* Origin of fast charging in hard carbon anodes. *Nature Energy* (2024). https://doi.org:10.1038/s41560-023-01414-5

35   Huang, W. *et al.* Onboard early detection and mitigation of lithium plating in fast-charging batteries. *Nature Communications* **13**, 7091 (2022). https://doi.org:10.1038/s41467-022-33486-4

36   Zeng, Y. *et al.* Extreme fast charging of commercial Li-ion batteries via combined thermal switching and self-heating approaches. *Nature Communications* **14**, 3229 (2023). https://doi.org:10.1038/s41467-023-38823-9

37   Konz, Z. M. *et al.* High-throughput Li plating quantification for fast-charging battery design. *Nature Energy* **8**, 450-461 (2023). https://doi.org:10.1038/s41560-023-01194-y

38   Yang, X.-G. & Wang, C.-Y. Understanding the trilemma of fast charging, energy density and cycle life of lithium-ion batteries. *Journal of Power Sources* **402**, 489-498 (2018). https://doi.org:https://doi.org/10.1016/j.jpowsour.2018.09.069

39   Yang, X.-G., Liu, T. & Wang, C.-Y. Thermally modulated lithium iron phosphate batteries for mass-market electric vehicles. *Nature Energy* **6**, 176-185 (2021). https://doi.org:10.1038/s41560-020-00757-7

40   Wang, C.-Y. *et al.* Fast charging of energy-dense lithium-ion batteries. *Nature* **611**, 485-490 (2022). https://doi.org:10.1038/s41586-022-05281-0